Integrated hydrologic model calibration under non-stationary climates

by

Mohan Song

A thesis

presented to the University of Waterloo

in fulfillment of the

thesis requirement for the degree of

Master of Science

in

Earth Sciences (Water)

Waterloo, Ontario, Canada, 2024

Author's Declaration

I hereby declare that I am the sole author of this thesis. This is a true copy of the thesis, including any required final revisions, as accepted by my examiners.

I understand that my thesis may be made electronically available to the public.

Abstract

With global climate change, quantifying water availability for management under non-stationary conditions is, and will continue to be, a major challenge. When hydrologic models are calibrated to historic climatic conditions, they may lack the ability to simulate future extreme climates. This research quantified changes in model calibration under non-stationary climate conditions using the Harold L. Disney Training Center (HLDTC) site in Kentucky, USA for demonstration. An integrated hydrologic model of the site was developed using HydroGeoSphere (HGS) and was calibrated using PEST. Hydraulic conductivity (K), specific storage (Ss), and surface friction coefficient parameters were calibrated under four different climate scenarios based on two moderately-extreme precipitation events during the observation period: a. the entire observation record, including the two moderately-extreme precipitation events (base scenario), b. the entire observation record minus the short duration event (April 2017), c. the entire observation record minus the long duration event (February 2018), and d. the observation record without either event. The results demonstrate that the inclusion of observations from extreme precipitation events impact the calibration of the hydrologic model. The variations in K and Ss were the highest between scenarios of all the calibration parameters tested, while the ridge surface friction, topsoil hydraulic conductivity, or clayey sand specific storage remain unchanged. K has the greatest decrease in lateral K (x and y direction) of the clayey sand layers in Scenario D, and greatest increase in lateral K of fractured rock formation in Scenario C. This indicates the importance of lateral flow in the fractured rock during the shorter duration precipitation event. Ss changed in the fractured rock formation in Scenario B, indicating the importance of storage in the fractured rock during the longer duration precipitation event. The model constructed by this study can better capture shorter duration moderately-extreme precipitation events, demonstrated by a better match between observed and simulated hydraulic heads in Scenario C. The results also suggest that not only the presence or absence of these events informs model calibration, but the timing and duration of these events influences the parameters it informs.

Acknowledgements

I would like to express my gratitude to all those who helped me during the writing of this thesis.

The deepest and most sincere gratitude is extended to my advisor, Dr. Andrea Brookfield, for her inspiring insights and continuous support of my research over the past two years. As the guide of my academic journey, she used her patience and experience to lead me through my master's project research and gradually mastered the skills of academic research. She took me on field trips to the study site, which enabled me to gain a more visualized concept of my model. I also attended my first academic conference with her, which gave me new insights into cutting-edge research in hydrogeology. I am also extremely grateful to my other committee members, Dr. Alan Fryar and Dr. Colby Steelman, for their suggestions on my research. Thanks to Alan for his warm hospitality in Kentucky and for showing me around the study site.

Special thanks to my family in China. Although the pandemic did not allow me to be with them a lot, they never stopped supporting me in their own ways.

This thesis marks the end of my master’s research, but I believe it is also the beginning of my next journey. Once again, I would like to take this opportunity to express my sincere gratitude to everyone who has encouraged and supported me throughout this journey.

Table of Contents

List of Figures

List of Tables

Chapter 1
Introduction

Fresh water, which occupies only 2.59% of the world's water resources, is the foundation on which humans and all life depend (USGS, 2019). Of this, only 23% of water resources, including groundwater and surface water, are accessible (USGS, 2019). Over the past few decades, as the population increased, the water demands of industry and agriculture also increased. It is predicted that by 2050, industrial water demand will grow more rapidly than agricultural water, especially in less developed regions such as Africa (Boretti & Rosa, 2019). However, the total amount of fresh water available to humans will further decrease, which will exacerbate the problem of water scarcity everywhere. Therefore, the establishment of long-term water resources management systems will continue to be an issue of concern.

Climate change is also a major environmental issue confronting the world and water management, particularly extreme climatic events. Weather observations in recent years show that some regions are experiencing a trend of increasing frequency of rainfall with temperature, such as in India (Meehl et al., 2000). The same trend has been found in the Netherlands, where scientists have shown that although the increase in temperature has reduced the frequency of extreme cold events which is beneficial to agriculture, the increase in extreme precipitation events can still have a negative impact on crops (Powell & Reinhard, 2016). Thus, it has become evident that we must consider extreme climate conditions in water resources management planning.

Numerical modelling is a common approach for supporting water resources management. Models can estimate groundwater and surface water availability over time by combining existing aquifer properties, geological settings, surface properties, and climatic factors into the governing equations for surface water and groundwater movement. However, there are always inaccuracies between model predictions and actual measurements. These inaccuracies are caused by the simplification of the conditions and processes represented in the models, either to facilitate calculations and computations or due to a lack of data. At the same time, extreme events that are associated with climate change, such as floods and droughts, may cause bias in predictions due to their uncertainty in its intensity and duration (Schewe et al., 2019).

Climate predictions are very uncertain, and this includes uncertainty in the prediction of the frequency and intensity of extreme events, which can then cause significant uncertainty in predicting the hydrologic response to the events. In addition, as future climates are predicted to be much different than past climates, there are concerns that hydrologic models calibrated using historic climate conditions may not be able to simulate future conditions. As such, it is important to consider the impact of this non-stationarity on hydrologic models and their ability to simulate the hydrologic response to extreme climatic events (Holman et al., 2011). There are several challenges associated with identifying and quantifying this impact, including underlying model assumptions and uncertainty, and uncertainty in the model parameters and observed data used to calibrate these models.

There is also uncertainty associated with how climate conditions are incorporated or coupled to hydrologic models (Grimaldi et al., 2019). With one-way feedback between climate and hydrology there is a disconnect between the climate conditions and the hydrologic conditions – the climate cannot respond to changes in hydrology. To enable climate simulations in hydrologic models, coupling a hydrologic model with one or more climate models is often required. Due to the differences in parameters, model structure, etc. between models, large uncertainties may arise when simulations are performed with the coupled model, especially for large-scale sites (Grimaldi et al., 2019).

It is evident that holistic approaches are necessary to assess hydrologic responses to climate change; however, computational efficiency is necessary. While there remain issues related to coupling of climate and hydrology, integrated hydrologic models that can capture surface water and groundwater flow and transport conditions are readily available. An integrated hydrologic model incorporates surface water, groundwater, and the interactions between them and is more capable of simulating hydrologic responses to extreme events than models that simulate the surface or subsurface flow conditions separately. However, what remains uncertain is how well an integrated model, calibrated under historic conditions, can simulate extreme events which are outside of the range of the data used to calibrate and validate the model.

The objective of this study is to quantify changes in model calibration under non-stationary climate conditions using the Harold L. Disney Training Center (HLDTC) site in Kentucky, USA for demonstration. Recent work by Sherman (2019) provides hydrological characterization of the site, in addition to hydrologic data collected during recent moderately-extreme flood events at this site. In this work, this data is used to develop and calibrate an integrated hydrologic model of the site using HydroGeoSphere. The model is calibrated with and without recent moderately-extreme climate events to identify how calibrated parameters and model results vary, identifying and quantifying the importance of incorporating extreme climate events into hydrological models.

Chapter 2
Background

This research uses the integrated hydrologic model, HydroGeoSphere (HGS), to model the study site, the Harold L. Disney Training Center (HLDTC) in Kentucky, USA. In the following sections, details about the site and model selection are provided.

2.1 Study site

The Harold L. Disney Training Center (HLDTC) is operated by the Kentucky Department of Military Affairs located in Knox County, Kentucky, and is adjacent to the town of Artemus (Fig. 1). The Köppen climate classification of the region is defined as humid subtropical, characterized by hot and humid summers (average high temperature of 30°C in July), and relatively mild winters (average low temperature of -4.9°C in January) (Sherman, 2019). The annual average temperature of Artemus, Kentucky is 13.3°C, and the annual average precipitation is 1275 mm (Weatherbase, 2022). The area experiences an average of 123 days of precipitation throughout the year. The most frequent rainfall is in March (11.8 days) while the most frequent snowfall is in January (1.8 days) (Weatherbase, 2022).

The site is surrounded by the Cumberland River on three sides and a ridge on the southern border (Fig. 1; Sherman, 2019). The site is used primarily for military and government training exercises and crop cultivation. Based on satellite photos and field observations, the vegetation in the study area can be roughly categorized into two types: crops (corn and soybeans) in the floodplain, and forest that surrounds the cultivated land. The crops are planted in June and harvested in October and November, for soybean and corn respectively. It also follows a routine that corn is planted in even years, while soybean is planted in odd years (G. Disney, personal communication).

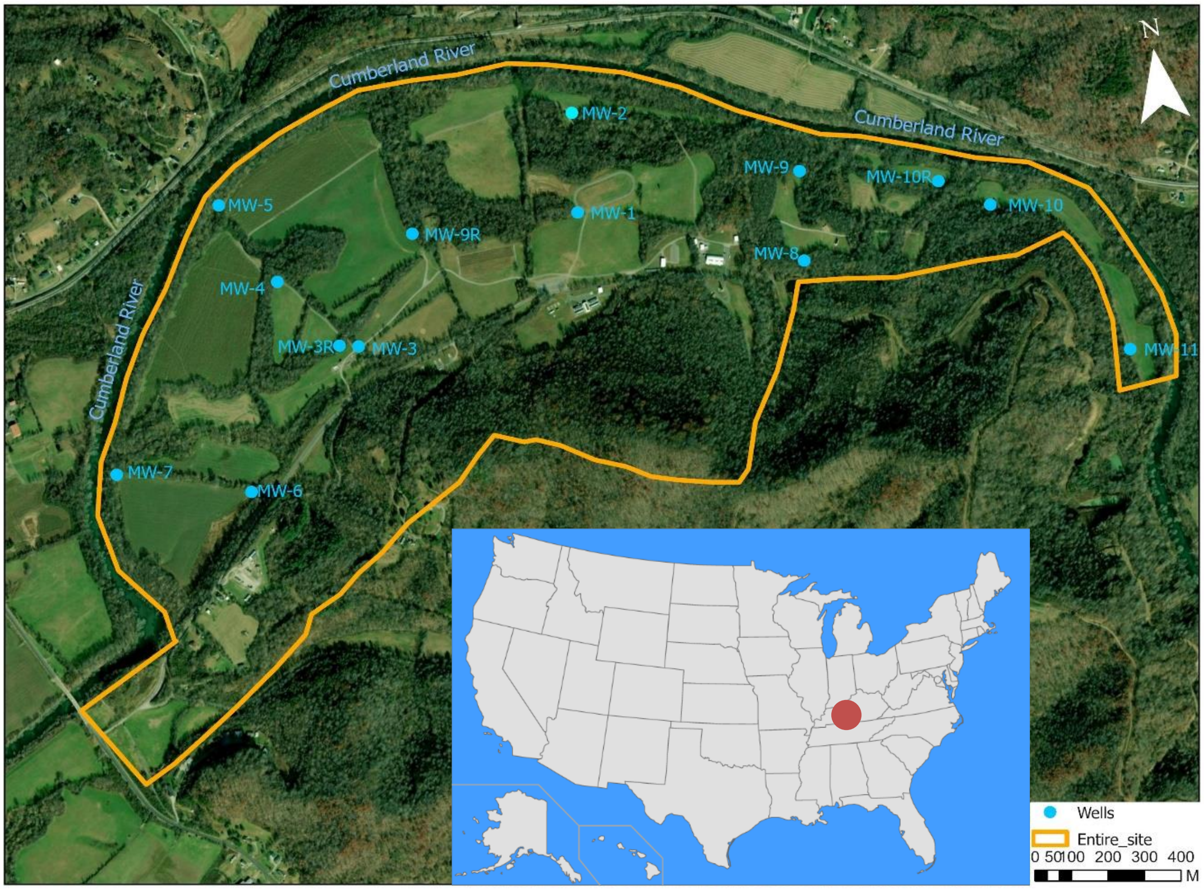

Fig. 1 Location and map of the HLDTC site in USA. The orange line is the HTDTC boundary, with the monitoring wells indicated by the blue symbols. (Modified from: Sherman, 2019); inset retrieved from: www.sporcle.com)

Located in the Eastern Coal Field Region, the alluvium, including flood plain and low-level terrace, is comprised of silt, clay, sand, and gravel (Sprinkle et al., 1983). The Pennsylvanian Breathitt Formation is one of the major formations underlying the area (Fig. 2) and most of the groundwater is stored in the fractures of the formation (Sprinkle et al., 1983). Three of the five subunits of the Breathitt Formation outcrop in the area, with the sub-basal unit forming the ridge on the southern edge of the site (Sherman, 2019).

The alluvium could provide adequate water quantities for local needs, but the water quality varies with depth (Sherman, 2019). Previous research indicated that, compared with river water, groundwater in the research site has higher concentrations of geogenic manganese and iron, which are higher than the drinking water standards in the National Secondary Drinking Water Regulations (NSDWRs); however, these elevated ion concentrations do not pose a health risk (Sherman, 2019). Though military activities frequently take place at the study site, these activities have not significantly impacted water quality (Sherman, 2019).

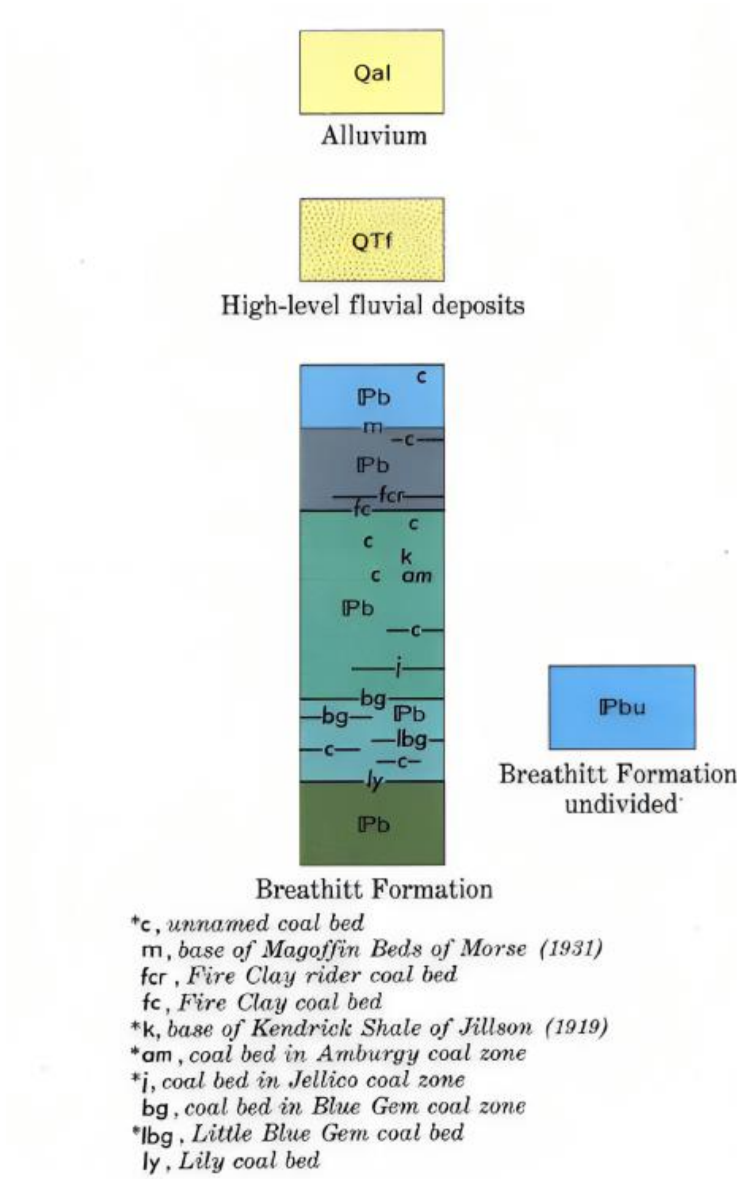

Fig. 2 Geologic cross-section of the study site. (Sherman, 2019)

Water samples were collected and analyzed from eleven monitoring wells and the Cumberland River quarterly from January 2017 to March 2018 (Sherman, 2019). Geological analyses such as soil core logs, grain size, carbon content, and mineral composition were also performed to better understand the geological setting and the hydraulic parameters. Water levels were hand-measured quarterly. In addition to this, pressure transducers were installed at MW-6 and MW-7 to measure hourly water levels and temperature, while the logged water levels were corrected for barometric pressure.

Water level measurements indicate that groundwater generally flows northward (from the ridge bottom toward the river), which is relatively consistent with the regional topography (Fig. 3) (Sherman, 2019). The shallowest groundwater levels based on the hydraulic head ranges are near the base of the ridge and are less than 1 mbgs (meters below ground surface), while the deepest groundwater levels are near the riverbanks are greater than 4.5 mbgs (Sherman, 2019). The water levels at HLDTC also fluctuate seasonally, with higher water levels in the spring and lower water levels in the fall (Sherman, 2019). It was found that the chemical composition of the groundwater is similar to that of precipitation, which indicates that precipitation is the main source of groundwater recharge.

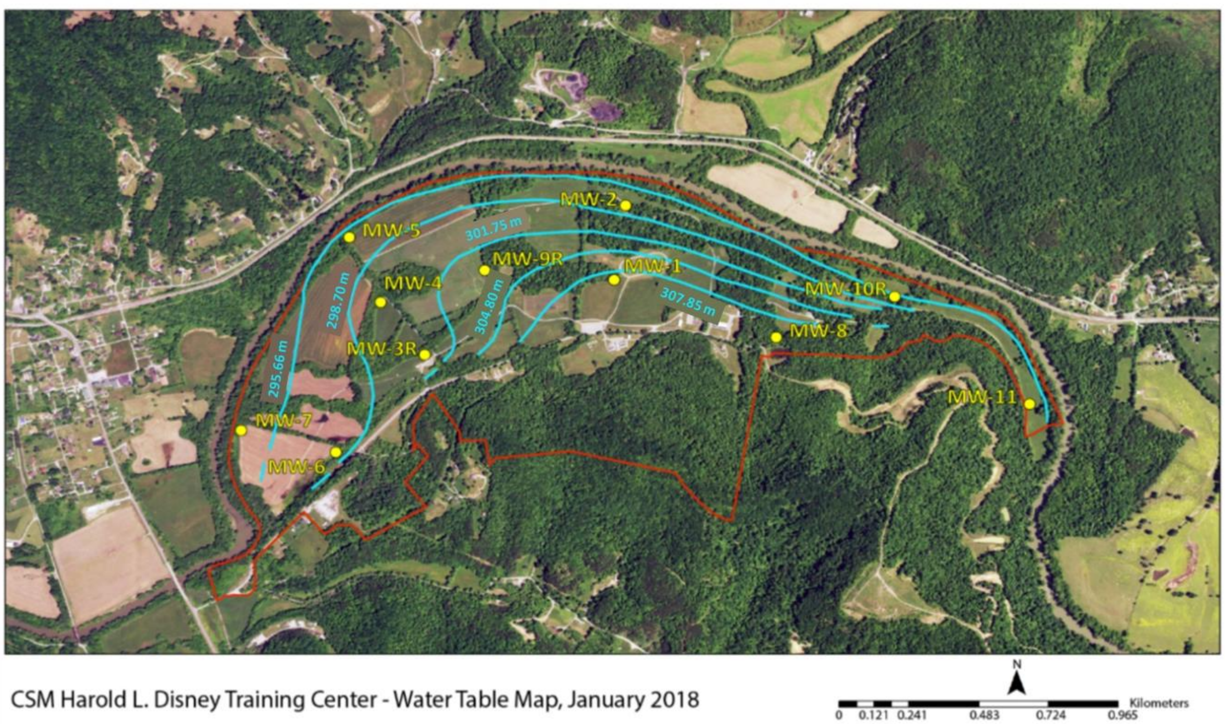

Fig. 3 HLDTC water table map, January 2018 (Sherman, 2019)

For aquifer characterization, aquifer tests and sieve analyses were conducted to estimate hydraulic parameters. The estimated hydraulic conductivity (K) values from sieve analyses ranged from 0.002 to 0.015 cm/s (Table 1), and are consistent with typical ranges for silty sands, fine sands, and well-sorted sands (Sherman, 2019). Estimates of K from slug and pumping tests were generally lower, ranging from

4.85×10^{-6}–1.00×10^{-3} cm/s, and are consistent with typical ranges for silt, silty sands, and well-sorted sands (Sherman,2019).

Table 1 HLDTC HydrogeoSieveXL hydraulic conductivity (K) estimates of the wells within the greater study area (Modified from: Sherman, 2019)

Well ID	MW-3R-3	MW-3R-4	MW-4-3	MW-4-4	MW-4-5	MW-5-4
Mean Value (m/s)	4.82E-05	6.58E-05	8.65E-05	1.82E-04	3.76E-05	6.70E-05
Well ID	MW-5-5a	MW-5-5b	MW-5-6b	MW-7-5	MW-7-7b	
Mean Value (m/s)	6.95E-05	5.31E-05	6.40E-05	2.06E-05	3.42E-05	

2.2 Hydrologic Model

There are a number of integrated hydrological models available that could be applied to this site, including ParFlow (Maxwell et al., 2023), CATHY (CATchment HYdrology) (Camporese et al., 2010), GSFLOW (Regan & Niswonger, 2021), and HydroGeoSphere (HGS) (Aquanty Inc., 2018). ParFlow is an integrated hydrologic model that simulates surface and subsurface water movement using the Richards equation, applying multigrid-preconditioned Newton–Krylov methods to perform three dimensional simulations of variably saturated subsurface flow in heterogeneous porous media (Maxwell et al., 2023). ParFlow has been used to simulate a wide range of applications such as hydrologic response to climate projections, reactive transport, and land-water energy balancing (Kuffour et al., 2020). Parflow is generally applied to large-scale systems, providing high-resolution surface and groundwater simulations up to continental scales, such as Naz et al. (2023) who developed high-resolution hydrologic models of continental Europe, coupling ParFlow with Common Land Model (CLM). In this work, the ParFlow-CLM model presented a relatively good performance in terms of estimating evapotranspiration, topsoil moisture, and groundwater storage (Naz et al., 2023). Other recent research includes work by Yang et al. (2023), who further advanced the ParFlow model developed for the contiguous United States (CONUS-ParFlow) to better represent continental-scale water source problems such as impacts of climate change on groundwater in the United States. Similar to the work by Naz et al. (2023), this study also used the CLM model to provide the required atmospheric and environmental inputs to ParFlow (Condon & Maxwell, 2019). The model developed by Yang et al. (2023) provides a more accurate description of topography and hydrostratigraphy resulting in better simulation of surface water-groundwater interactions and variations.

CATHY (CATchment HYdrology) is an integrated hydrological model that focuses on catchment-scale simulations. CATHY is a finite difference model that uses the 3-D Richards equation for subsurface flow and the diffusion-wave version of St. Venant's equation for surface flow (Camporese et al., 2010). CATHY can extract and construct conceptual drainage networks from DEM files, simulating the flow and solute transport under different topographies (Camporese et al., 2010). Niu et al. (2014) developed a tool to simulate lake dynamics and flash floods using CATHY, which are critical components of climate change modeling. CATHY is also coupled to the land surface model (LSM), NoahMP, which provides more detailed simulations of precipitation and vegetation than other LSMs, thus providing more accurate climate inputs to hydrologic models (Niu et al., 2014).

GSFLOW is also a widely used integrated hydrologic model that integrates USGS Modular Groundwater Flow Model (MODFLOW) and USGS Precipitation-Runoff Modeling System (PRMS) (Markstrom et al., 2008). The subsurface flow is simulated in MODFLOW with the Richards equation using finite difference (Harbaugh, 2005), while surface water flow (precipitation, evapotranspiration, surface runoff, etc.) is simulated by hydrologic response units (HRUs) and water routing in the PRMS algorithm (Markstrom et al., 2008). Wu et al. (2019) applied GSFLOW to water resources management in the arid zone of Northwest China. Combining DEM data as well as the meteorological data from local weather stations, the model was calibrated with manually adjusted parameters (Wu et al., 2019). By applying the calibrated model to nine CMIP5 climate scenarios, the study found that the future water resources changes in the Zhangye Basin area are problematic under the current level of agricultural activities (Wu et al., 2019).

HydroGeoSphere (HGS) is the integrated hydrological model that was selected for this research (Aquanty Inc., 2018). HGS uses the control-volume finite element method or finite difference approach to simulate coupled surface and subsurface flow and transport (Aquanty Inc., 2018). A modified Richards equation is used to simulate the three-dimensional transient subsurface flow in a variably saturated porous medium (Equation 1: Aquanty Inc., 2018).

$$-\nabla \cdot (w_m q) + \sum \Gamma_{ex} \pm Q = w_m \frac{\partial}{\partial t}(\theta_s S_w)$$
$$q = -K \cdot k_r \nabla(\psi + z) \tag{1}$$

w_m = volumetric fraction of the total porosity occupied by the porous medium [-]

q = flux [L T^{-1}]

Γ_{ex} = volumetric fluid exchange rate [L^{3}L^{-3}T^{-1}]

Q = fluid exchange with the outside of the simulation domain [L^{3}L^{-3}T^{-1}]

θ_s = saturated water content [-]

S_w = degree of water saturation term [-]

K = hydraulic conductivity [L T^{-1}]

k_r = the relative permeability of the medium [-]

ψ = pressure head [L]

z = elevation head [L]

For surface water flow, HGS uses the diffusion wave version of the Saint Venant equation for depth-integrated surface water flow (Equation 2: Aquanty Inc., 2018).

$$\frac{\partial \phi_0 h_0}{\partial t} - \frac{\partial}{\partial x}\left(d_0 K_{0x} \frac{\partial h_0}{\partial x}\right) - \frac{\partial}{\partial y}\left(d_0 K_{0y} \frac{\partial h_0}{\partial x}\right) + \mathrm{d}_0 \Gamma_0 \pm Q_0 = 0 \tag{2}$$

ϕ_0 = surface flow domain porosity [-]

h_0 = water surface elevation [L]

t = time [T]

d_0 = depth of flow [L]

K_{0x}, K_{0y} = surface conductance [L T^{-1}]

$\mathrm{d}_0\Gamma_0$ = volumetric flow rate per unit area [L T^{-1}]

Q_0 = volumetric flow rate per unit area [L T^{-1}]

HGS has been applied to many water resource problems, including both small-scale and large-scale simulations, making it relevant for this work. Lü et al. (2021) simulated runoff to the Shiguan River basin in China by integrating HGS with different precipitation modules. Results of the study suggest that the simulated annealing (SA) approach is preferable for representing precipitation patterns in HGS, especially for depicting flood peaks in large-scale watersheds (Lü et al. 2021).

The work by Davison et al. (2018) is an example of HGS application on a larger scale. In this work, HGS was coupled with a weather prediction model, the Weather Research and Forecasting (WRF) model. This coupled model was applied to the California Basin, simulating a ten-day period. The study identified a connection between the water table level and surface latent heat fluxes in the region and also suggested that the HGS-WRF model can save computational costs compared to traditional basin-scale models (Davison et al., 2018).

HGS can be auto calibrated using PEST, a software package that automatically calibrates and performs uncertainty analyses for any numerical model (Doherty et al., 2021). PEST can provide more accurate parameter estimations because it removes user bias and is able to perform regularization both before the parameter estimation and during the inversion process (Doherty et al., 2021). An example of HGS coupled with PEST was conducted for the Waterloo Moraine in Ontario, Canada by Tong et al. (2021). To perform the hydraulic tomography analysis, the research applied and calibrated four geologic models using the coupled HGS-PEST model (Tong et al., 2021).

Chapter 3
Methods

This research focuses on the southwest corner of the HLDTC site, which is about one third of the entire site area and includes five monitoring wells (MW-3R, MW-4, MW-5, MW-6, MW-7) and one dry well (MW-3; Fig. 4). This model domain includes the streambank, floodplain and part of the ridge and was selected due to the relatively higher density of monitoring wells, which provides characterization data, and high-resolution water level data at MW-6 and MW-7 for calibration.

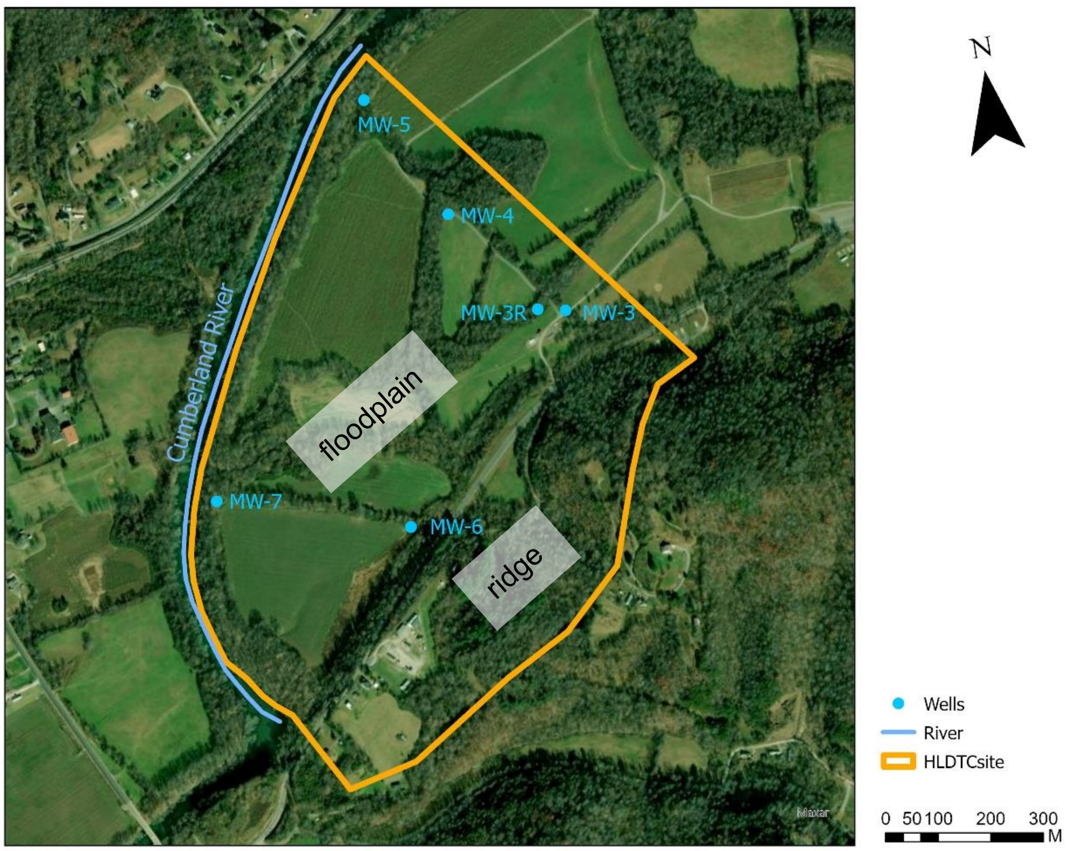

Fig. 4 Model domain at the HLDTC. The orange line is the study area boundary, with the monitoring wells indicated by the blue symbols. (Modified from: Sherman, 2019)

3.1 Mesh Generation

The mesh was generated with Algomesh (version: 2.0.20.32621, x64) (Merrick & Merric, 2016) and it accurately represents the well locations, streambed, and ridge features (Fig. 5). The topography of the study area was imported into Algomesh using the regional elevation data acquired from U.S. Geological Survey (USGS) (2017; Fig. 5). To ensure stable model simulations, the DEM data were smoothed to accommodate sudden changes in topography (e.g., cliffs) along the ridge. The mesh was refined in regions of topographical change, subdividing the channels, floodplains, and ridges (Fig. 6).

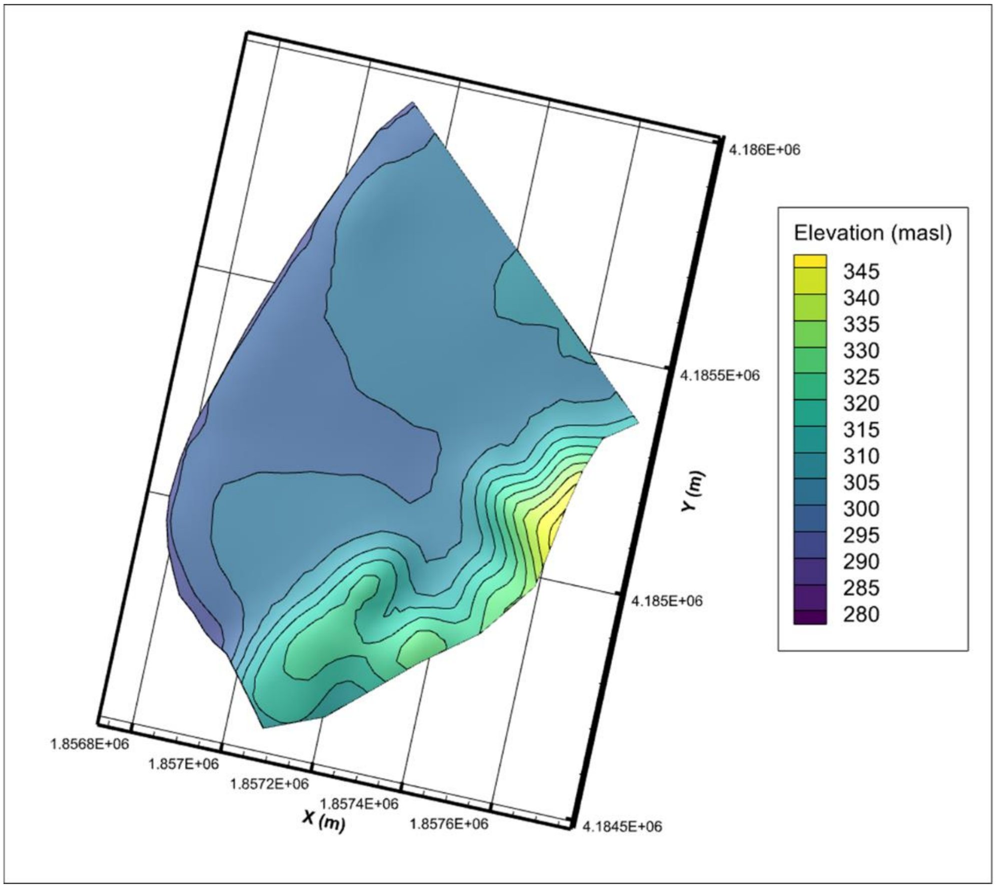

Fig. 5 Elevation data of the study area in meters above sea level. The orange line is the study area boundary. (Modified from USGS, 2017; present in Tecplot)

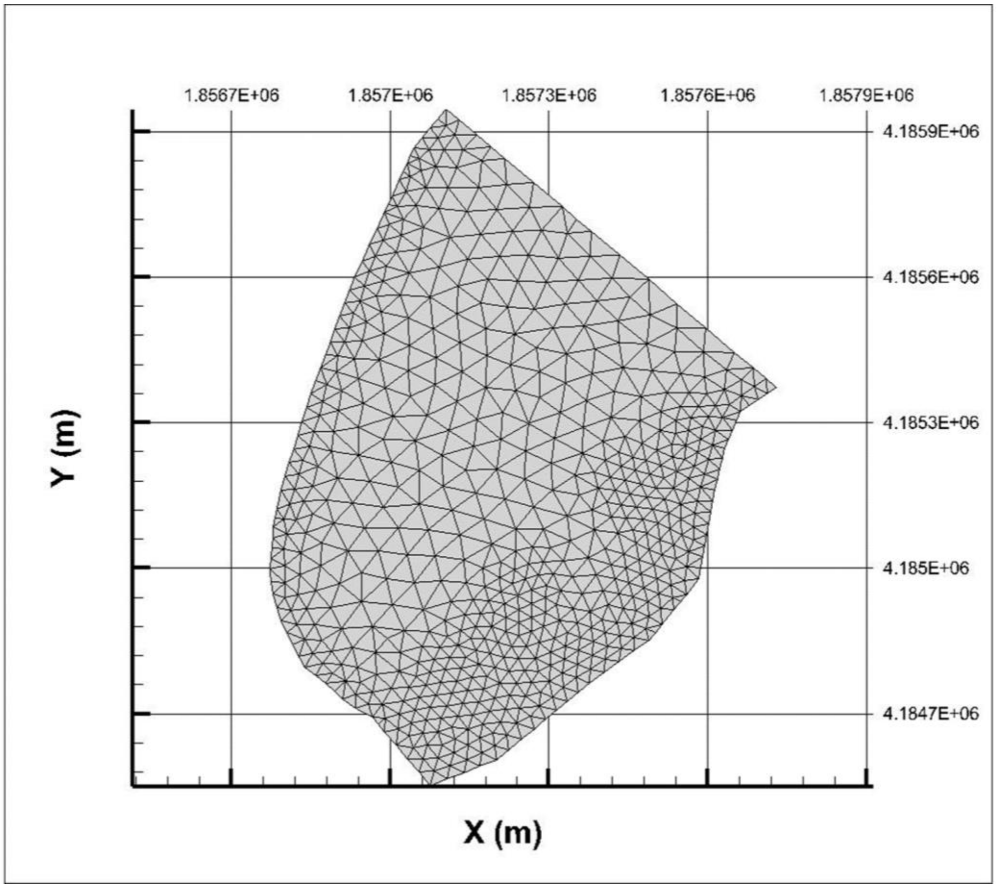

Fig. 6 Mesh developed of the HLDTC site with Algomesh (present in Tecplot).

The geologic model was constructed in HGS using multiple layers of various thicknesses. Field observations including well logs (Appendix A; Appendix B) and a schematic diagram (Fig. 7) from Sherman (2019) provide detailed information on the composition and thickness of each layer, as well as the initial static water level at the time of well installation. Based on these observations and the USGS elevation data, the 3D mesh is divided into 18 layers consisting of four layers that are 0.25 m thick, followed by four layers that are 2.25 m thick, then two 1 m thick layers which allow for accurate representation of the depth of water level measurements, and finally three 2 m thick layers, from top to bottom. This vertical discretization was selected to capture the groundwater flow dynamics of the site and remain computationally feasible. These subsurface layers are assigned to three lithological zones, starting with the base of the model located 18 meters below ground surface. This depth was selected to be deep enough to minimize the influence of the bottom boundary condition on the local flow paths. The layers above the bottom boundary are a weathered rock with a thickness of 10.25 m, overlain by a clayey sand layer of a thickness of 7.5 m, which is overlain by a 0.25 m thick topsoil. The surface of the domain is also divided into two zones, the ridge and the flood plain, which is consistent with the mesh generation and with the different land cover types at this site. Overall, the mesh has 8359 nodes, with 643 nodes per layer and 13 layers of varied thickness.

3.2 Boundary conditions

The model has incorporated stream, climate, and hydrogeological data to constrain boundary conditions on the surface and in the subsurface of the model.

3.2.1 Surface boundary conditions

Boundaries applied to the surface of the model include those constraining river flow, overland flow, and precipitation. The boundary condition at the river varies with time; unfortunately, there is no measured streamflow available along the section of the Cumberland River in the study area. Therefore, data from the closest gage stations located upstream and downstream of the study site were used to estimate river height along the site within the study period.

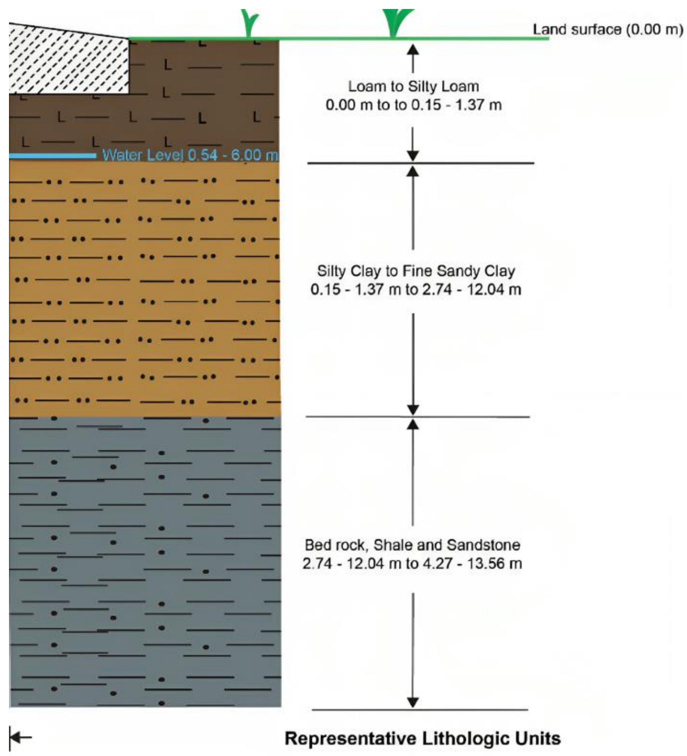

Fig. 7 Schematic diagram of HLDTC lithology. (Sherman, 2019)

The closest USGS monitoring stations with streamflow data available during the observation period along the Cumberland River are Pineville (03402900) which is upstream of the HLDTC site and Barbourville (03403500) which is downstream. Additionally, high resolution elevation data of the streambed for the length of the river between these gages was acquired from KyFromAbove (2022). To interpolate the river depth along the model domain, the gradient of water level change between the gage station was calculated based on change in streambed elevation following:

$$\Delta = \frac{G_P - G_B}{E_P - E_B} \tag{3}$$

G_P = gage height from Pineville

G_B = gage height from Barbourville

E_P = elevation near Pineville

E_B = elevation near Barbourville

This gradient was calculated daily and was applied to the length of the river within the model domain to determine the surface boundary condition.

The remaining lateral surface boundaries are set as critical depth boundary conditions, allowing water to leave the model domain if the surface hydraulic gradient is towards the boundary, but not allowing water to enter the domain.

The model's top boundary condition is calculated as precipitation minus estimated evapotranspiration (ET), and therefore represents only the portion of precipitation contributing to surface runoff and groundwater recharge. This approach was taken to reduce the computational burden of the model and the parameterization required for the ET module. The precipitation data used for this boundary is consistent with Sherman (2019) and is measured every 30 minutes at the Pineville and Barbourville gage stations. Daily precipitation for the two sites was averaged for model input. ET was removed from precipitation for the top boundary. Although the vegetative land cover is variable across the site and varies with time (higher in summer and fall, lower in winter and spring), a constant ET of 60% of precipitation was used for this work (Kentucky Geological Survey, n.d.) due to the computational limitations. This approach ignores all the factors that cause temporal and spatial variation of ET, including air temperature, soil moisture and solar radiation, and future work should include estimates of ET that vary spatially and temporally with these changing conditions. However, since the site is not located at the headwaters of the basin, the river boundary conditions integrate the effects of varying ET as the river responds to the basin conditions, including the partitioning of precipitation. The river boundary is based on observed data and changes on a daily basis, and so the river gage height does represent the upstream basin response to variations in ET.

3.2.2 Subsurface boundary conditions

The subsurface boundaries of the site consist of the boundary below the river, the bottom boundary, and the remaining lateral boundaries. Given the multiple layers of the subsurface river boundary, it is difficult to specify temporally-variable water levels as the surface boundary does. Therefore, all the subsurface river nodes are assigned the daily average water level of the surface river boundary. This assumes that the subsurface immediately below the river is fully saturated and is in equilibrium with the river.

The remaining lateral subsurface boundaries are set as no-flow boundary conditions, due to a lack of information about lateral groundwater flow movement, making the river the main subsurface boundary constraint of the model.

To ensure numerical stability, precipitation increased by 1 x 10^{-12} m/s to avoid timesteps with no precipitation. A constant flux boundary of 1 x 10^{-12} m/s was assigned to all bottom nodes to eliminate the precipitation input error caused by HGS while creating downward flows which are more consistent with the actual environment.

3.3 Initial Conditions

The model requires initial conditions for simulation, and spin-up runs are needed to generate these initial conditions for integrated hydrologic models. This ensures that the initial surface and subsurface hydrologic conditions are in equilibrium. Spin-up runs used average climate conditions and constant river and subsurface boundary conditions.

For the spin-up model, the river (surface and subsurface) boundary conditions are set to the average steady state value over the observed period (January 05, 2017, to March 10, 2018), while the precipitation boundary is set to a value similar to the long-term precipitation average minus ET. A detailed table of the model set up including the spin run model can be found in Table 2. Results of the spin-up run were consistent with field measurements reported by Sherman (2019) and provide a reasonable initial condition for the transient simulations (Fig. 8).

Table 2 Boundary conditions applied for both the spin-up and the transient simulations.

Boundary	**Spin-up Model**	**Transient Model**
River (surface)	291.0 m	298.3 – 299.4 m
River (subsurface)	290.3 m	290.3 – 299.4 m
Ridge (surface)	Critical depth	Critical depth
Ridge (subsurface)	No flow	No flow
Sides (surface)	Critical depth	Critical depth
Sides (subsurface)	No flow	No flow
Bottom (subsurface)	1E-12 m/s	1E-12 m/s
Precipitation (excluding ET)	1E-08 m/s	0 – 3.35E-7 m/s

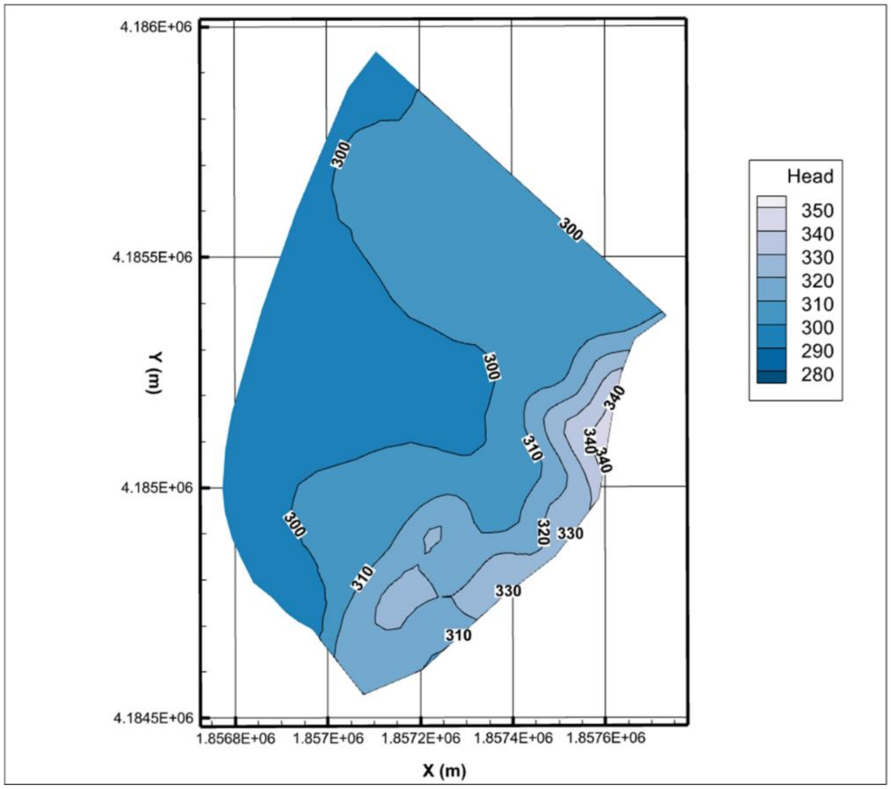

Fig. 8 Model simulation result for January 05, 2017, present in Tecplot 360

3.4 Model Calibration

The model is automatically calibrated using PEST (version 17.5, 32-bit) to best match observed water level data from monitoring wells MW-6 and MW-7. Calibration parameters are hydraulic conductivity (K), specific storage (S_S), and surface friction coefficients for various layers and regions in the domain. The subsurface properties, K and S_S, were selected to vary in response to changes in the climatic inputs, allowing groundwater flow conditions to vary. For surface water flow, the surface friction coefficients were allowed to vary and were the only surface parameter in this model available for calibration. Initial values and calibration ranges (Table 3) for all parameters are selected from either previous literature for the formation or surface type, or previous field work from the study site. As a result of preliminary model simulations, the initial values for hydraulic conductivity are larger in the vertical direction compared to lateral. While this was not expected, it is feasible that fracture orientation in the bedrock in addition to shrinkage and cracking in the clayey layers could cause this level of anisotropy. PEST is constrained with parameter ranges that are consistent with site characteristics and measurements provided by Sherman (2019) (Table 3).

Table 3 Calibration parameters and ranges for PEST

Calibration Parameter	**Initial value**	**Minimum value**	**Maximum value**	**Source**
Floodplain (friction, isotropic)	0.038	0.010	0.100	Aquanty Inc. (2018)
Ridge (friction, isotropic)	0.015	0.010	0.100	Aquanty Inc. (2018)
Topsoil (K, m/s, isotropic)	2.67E-4	5.0E-5	5.0E-4	Sherman (2019)
Clayey sand (K, m/s, X/Y)	5.0E-6/5.0E-6	1.0E-6/1.0E-6	1.0E-4/1.0E-4	Sherman (2019)
Clayey sand (K, m/s, Z)	1.0E-4	1.0E-6	1.0E-4	Sherman (2019)
Fractured rock (K, m/s, X/Y)	5.0E-5/5.0E-5	1.0E-6/1.0E-6	5.0E-4/5.0E-4	Sherman (2019)
Fractured rock (K, m/s, Z)	3.0E-4/3.0E-4	1.0E-6/1.0E-6	5.0E-4/5.0E-4	Sherman (2019)
Clayey sand (S_S, m^{-1})	1.62E-4	1.0E-5	5.0E-4	Sherman (2019)
Fractured rock (S_S, m^{-1})	8.0E-7	5.0E-8	5.0E-6	Sherman (2019)

Two moderately-extreme precipitation events occurred at HLDTC site during the measurement period in April 2017 and February 2018 (Fig. 9). The April 2017 event had one distinct hydrologic response to the precipitation event, while the February 2018 event had multiple distinct responses of varying stage heights. Both events are representative for moderately-extreme precipitation events in the region: the magnitude of the April 2017 event had occurred years prior in 2015 and 2003, while the February 2018 event was the second largest flood event within the region in the past 10 years. The base model for this research will be calibrated to the entire data record, and three additional scenarios will be simulated to quantify the impact of these events on calibrated parameters: one with the removal of the observations associated with the February 2018 event, one with the removal of the observations associated with the April 2017 event, and one with both events removed. The fit between observed and measured data and the calibrated parameters will be compared between each of these scenarios and the base case to determine what additional information the extreme precipitation events provided to the calibration process.

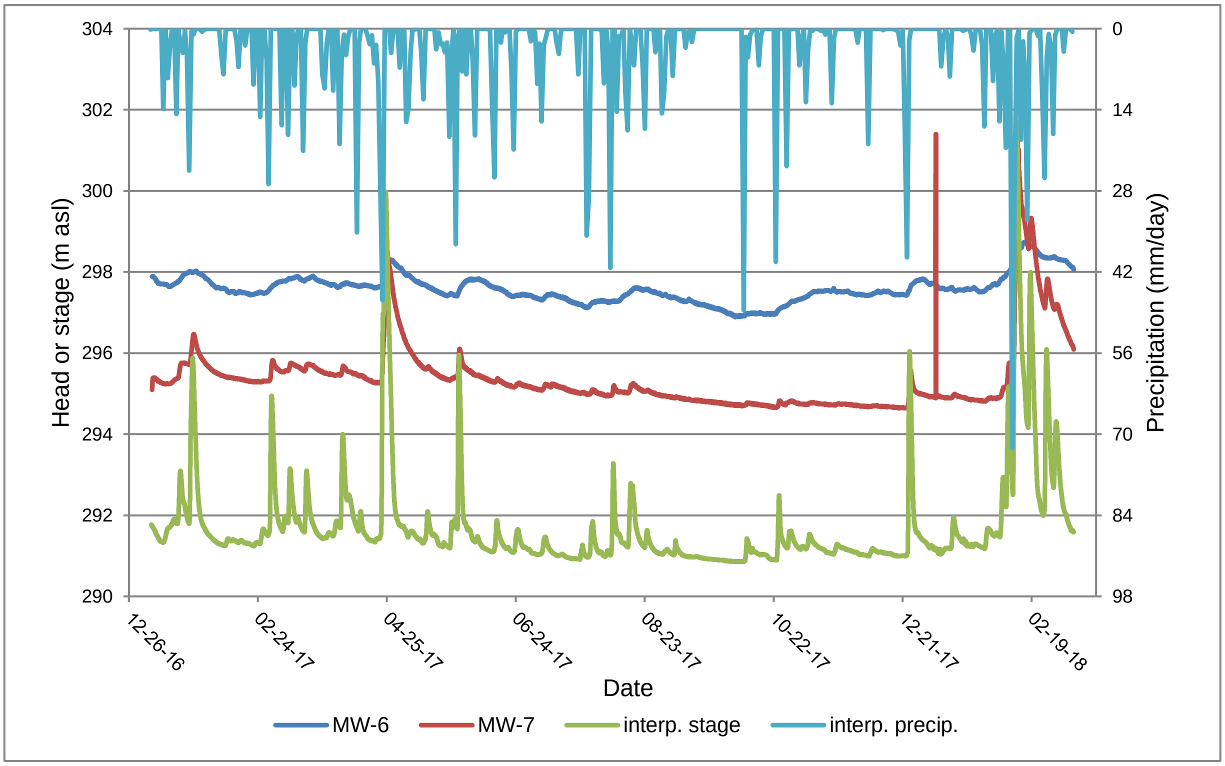

Fig. 9 HLDTC hydrographs for MW-6 and MW-7, with interpolated river stage, January 2017 to March 2018 (Sherman, 2019); average daily precipitation was averaged from USGS gage stations Pineville (03402900) and Barbourville (03403500)

Chapter 4
Results and Discussion

The PEST-calibrated HGS model of the HLDTC site was simulated for four different combinations of calibration datasets: **a.** the entire observation record, including the two moderately-extreme precipitation events (base scenario), **b.** the entire observation record minus the 1st event (April 2017), **c.** the entire observation record minus the 2nd event (February 2018), and **d.** the observation record without either event. In the spin-up simulation, the clayey sand layer was divided into three horizontal sublayers and the fractured rock layer was divided into two horizontal sublayers to capture any vertical differences in these units. Initial results indicate no differences in either unit, and so the model properties are considered uniform within the clay-sand layers and the fractured-rock layers.

Calibration results and parameters (Table 3) for the base scenario are compared to three alternative scenarios that exclude one or both moderately-extreme precipitation events. Comparison of the model results and calibrated parameters among the scenarios quantify the impact of these extreme events on the calibration process.

4.1 Base Scenario

The base scenario is calibrated with all the observed data, including the hydrologic response to the two moderately-extreme precipitation events. The calibrated parameters for the base scenario are provided in Table 4. Comparing the model results to the observations (Fig. 10), the simulated hydraulic heads for both observation wells are lower than the observed hydraulic heads (RMSE = 4.21). MW-7 shows a relatively high correlation ($R^2 > 0.9$) with the measured values and the timing of hydrologic response to precipitation events is consistent with observations. In both the observed data and model results, responses to precipitation events are strong in the winter and spring seasons, with a delay of about one day between the event occurrences and significant hydraulic head change. Conversely, in summer and fall, the hydrologic responses to precipitation events are weak, with small, lagged changes in hydraulic head. This seasonally shifting pattern of hydrologic response is likely related to the ET at the site. Vegetation and crops at the site increase ET during the summer and fall, while less vegetative coverage in winter and spring creates more rapid groundwater flow responses to precipitation events. Despite not capturing the temporal or spatial variations in ET in the model, these seasonal variations were still evident in model results because the river water levels also reflected the seasonal changes, with a larger change in river stage in response to precipitation events in the winter and spring compared to summer and fall. As MW-7 is located near the Cumberland River, the hydrologic response at this well is likely strongly influenced by river water levels. Therefore, the model was able to represent the seasonal variations in hydrologic response to precipitation observed at MW-7.

In contrast, the model has generally poor correlation to observed values at MW-6 ($R^2 < 0.1$, RMSE = 3.25). The model captures a response to only the two moderately-extreme precipitation events, and these hydrologic responses lag the precipitation event by more than ten days compared to measured values which respond within three days. In addition, the simulated hydraulic heads do not fall as rapidly as the observed values after the event. The error between the simulation and the observation is likely related to the simplification of the model. The model depicts the southern portion of the HLDTC site and, due to a lack of data to constrain them, has boundary conditions that ignore potential lateral groundwater flow through the site. MW-6 is located in the central part of the floodplain further from the river compared to MW-7. As a result, water level variations are likely influenced more by precipitation and lateral groundwater flow boundaries compared to MW-7 where the river boundary condition dominated the response. Due to a lack of data to constrain the lateral groundwater flow boundaries, the lateral movement of groundwater from outside of the domain (northeast) was ignored, thus the simulation results for MW-6 do not match the observations well. It should also be noted that the high RMSE value for both MW-6 and MW-7 reflect the lower simulated hydraulic heads compared to observations, presumably because the linear interpolation of the surface river boundary condition did not reflect the actual water level.

Table 4 Model calibration results for all simulated scenarios.

Calibration Parameter	**a. Two events**	**b. 2nd only (Feb 2018)**	**c. 1st only (Apr 2017)**	**d. No events**
Floodplain (friction, X/Y)	0.100/0.100	0.095/0.095	0.100/0.100	0.098/0.098
Ridge (friction, X/Y)	0.015/0.015	0.015/0.015	0.015/0.015	0.015/0.015
Topsoil (K, m/s, X/Y/Z)	2.7E-4/2.7E-4/2.7E-4	2.7E-4/2.7E-4/2.7E-4	2.7E-4/2.7E-4/2.7E-4	2.7E-4/2.7E-4/2.7E-4
Clayey sand (K, m/s, X/Y/Z)	4.3E-6/4.3E-6/9.1E-5	4.2E-6/4.2E-6/7.8E-5	4.3E-6/4.3E-6/7.8E-5	1.4E-6/1.4E-6/7.8E-5
Fractured rock (K, m/s, X/Y/Z)	4.5E-5/4.5E-5/2.6E-4	4.5E-5/4.5E-5/9.7E-5	1.2E-4/1.2E-4/8.0E-5	5.8E-5/5.8E-5/1.6E-4
Clayey sand (S_S, m^{-1})	1.62E-4	1.62E-4	1.62E-4	1.62E-4
Fractured rock (S_S, m^{-1})	7.83E-7	2.32E-6	7.83E-7	7.76E-7

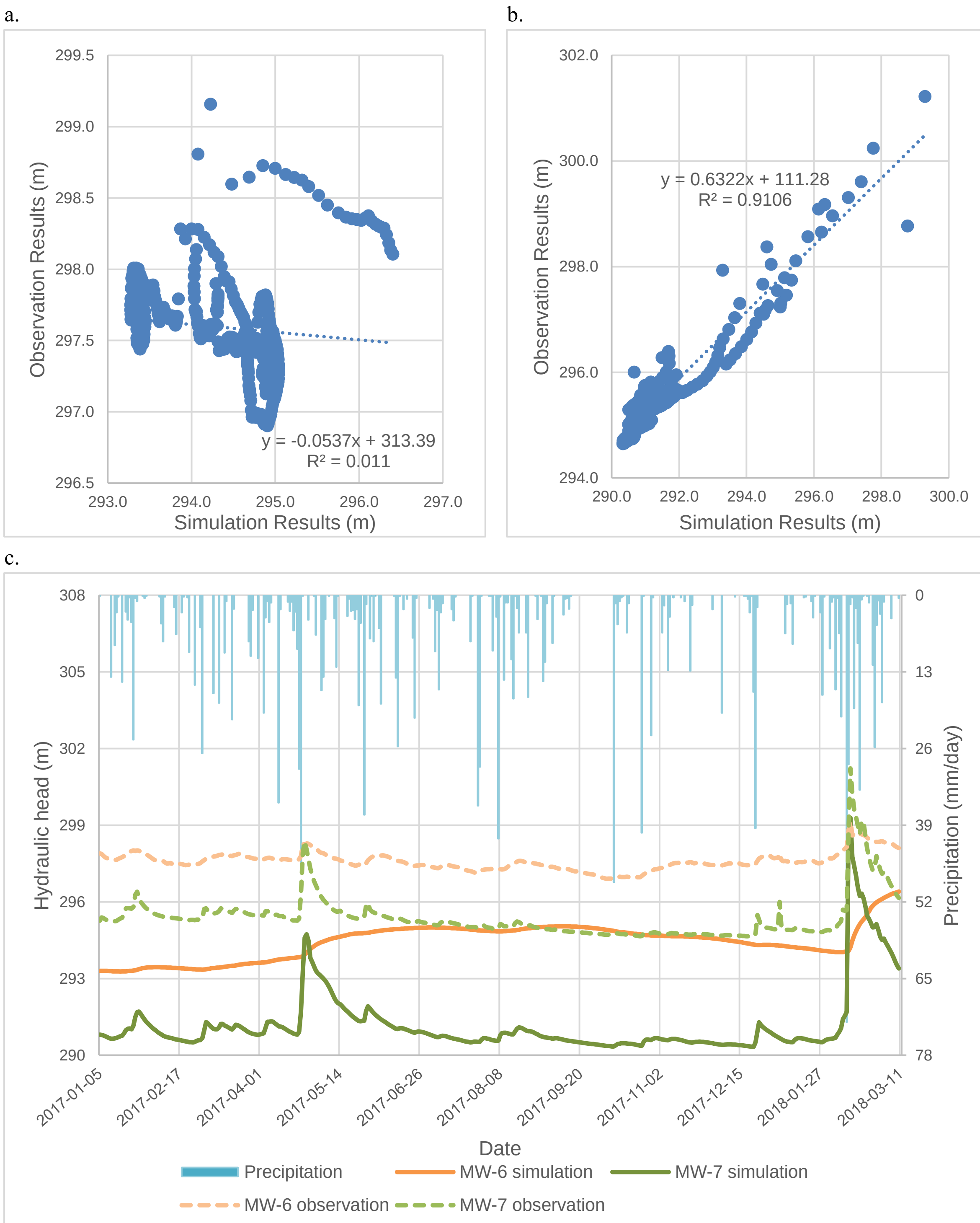

Fig. 10 Hydraulic head comparison between the model simulation based on the base scenario calibration and the observation from Sherman (2019) a. MW-6 b. MW-7 c. Hydrograph during the observation period with both data sets.

4.2 Alternative Scenarios

The HLDTC model was calibrated using PEST using three alternative scenarios with different combinations of the extreme hydrologic responses removed from the calibration dataset. Table 5 provides a summary of the percent change in calibrated parameters in the alternative scenarios compared to the base scenario.

Table 5 Percentage of parameter variation between base scenario and alternative scenarios (%)

Calibration Parameter	**b. 2nd only (Feb 2018)**	**c. 1st only (Apr 2017)**	**d. No events**
Floodplain (friction, isotropic)	-5%	0%	-2%
Ridge (friction, isotropic)	0%	0%	0%
Topsoil (K, m/s, isotropic)	0%	0%	0%
Clayey sand (K, m/s, X/Y)	-2%	0%	-67.4%
Clayey sand (K, m/s, Z)	-14.3%	-14.3%	-14.3%
Fractured rock (K, m/s, X/Y)	0%	+166.7%	-28.9%
Fractured rock (K, m/s, Z)	-62.7%	-69.2%	-38.5%
Clayey sand (S_S, m^{-1})	0%	0%	0%
Fractured rock (S_S, m^{-1})	+196.3%	0%	-0.9%

Of the parameters calibrated, and across all scenarios, the model was not sensitive to ridge surface friction, topsoil hydraulic conductivity, or clayey sand specific storage. Comparing the three alternative scenarios to the base scenario, the results indicate that the absence of one or more moderately-extreme precipitation events does impact the remaining calibration parameters to varying degrees.

Of all the parameters that did vary between scenarios, the surface friction coefficient for the floodplain changed the least, decreasing by 5% in Scenario B (containing only the February 2018 event) and by 2% in Scenario D (containing neither event). Compared to parameters that characterize surface properties, the calibration of subsurface properties is more sensitive to variations between scenarios. With respect to the clayey sand layers, K is reduced by 14.3% in the z-direction for all three alternative scenarios compared to the baseline. Lithologies are isotropic in the x and y directions. In scenarios B and C, which contain one event, K of clayey sand layer remain essentially unchanged in the x and y directions (Scenario B decreases by 2%), while in Scenario D, which has no precipitation events, the K in these directions decreases by 67.4% from the base scenario. So, when either of the events are removed (Scenarios B and C), the simulated water flow is slower vertically in the clayey sand formation. When both events are removed (Scenario D) the lateral flow is also limited, inferring both events captured faster lateral flow in the model. This indicates that the inclusion of these precipitation events provides information about faster flow conditions in all directions of the clayey sand units. The K values in the vertical direction are greater than those in the horizontal direction in all three alternative scenarios, which, as previously mentioned, could be a result of formation shrinkage and cracking. Future work should further study the anisotropy of this site, including seasonal changes and changes in response to dry and/or wet conditions.

Differing from the clayey sand layers, the fractured rock layers had variation in both K and S_S. For fractured rock hydraulic conductivity, scenarios B, C, and D all had relatively large variations from the base scenario. Scenario B and C had similar changes with a decrease of 62.7% and 69.2% respectively for K in the z-direction, demonstrating that both events are necessary to capture the faster vertical movement through this unit. Scenario C also had a 166.7% increase in K for the x- and y-directions, indicating that the first event provided more information about lateral movement in the fractured rock layer. Scenario D had the smallest change, with a 28.9% increase in K for the x- and y-directions, and a 38.5% decrease in K for the z-direction. In Scenarios B and D, K in the vertical direction and horizontal direction maintain the same relationship as in the base scenario (vertical value greater than horizontal value). This can indicate the vertical fracture orientation of the fractured rock layer. In Scenario C, due to the increase of K in the horizontal direction, its value is larger than that in the vertical direction, the water tends to flow horizontally more than vertically. Future work should also study the anisotropy of the fractured bedrock units to better inform these parameters. As for fractured rock S_S, Scenario B increased by 196.3%, which is the largest variation among all parameters, while Scenarios

C and D are essentially unchanged (0% and -0.9% respectively). Scenario B includes an event with a longer duration precipitation event, and the increase in storage indicates the need to have more water within the matrix to store that water as opposed to moving it within the domain. The variations in fractured rock formation K indicate that, compared to the base scenario, water flow is more oriented toward horizontal than vertical flow in all three scenarios. Compared to the base scenario, the inclusion of both moderately-extreme precipitation events provides more active hydrologic response in the fractured rock formation in the vertical direction, while the horizontal direction is limited.

The above analysis of the calibration results indicates that both the surface and subsurface calibrated parameters respond to the inclusion or exclusion of extreme precipitation events, with the subsurface response being more pronounced, and fractured rock having the most significant changes in calibration parameters of the subsurface layers. For the calibrated parameters, K is more sensitive to the inclusion of the extreme precipitation events compared to S_S, which also suggests that K has more uncertainty in the calibration process and that future work should focus on better constraining these parameters.

The intensity and duration of the extreme precipitation events also contribute to the differences in calibration results. The two events chosen for this study differed significantly in the amount of precipitation and the duration of the event, where the first event is more moderate in both aspects compared to the second (Fig. 9). Thus, the scenarios calibrating data from only one of these precipitation events (Scenario B and C) yielded different calibration datasets. Although the tendency of K in the z-axis direction (and in the horizontal direction for clayey sand) is similar in both scenarios, Scenario B, which contains only the large, longer duration precipitation event, has a dramatic increase in water storage in the fractured rock formation, while Scenario C, which contains only the shorter duration precipitation event, has a dramatic increase in lateral water flow in the fractured rock formation. Summarizing above findings with precipitation and river gage data, it can be inferred that watersheds respond and recover more quickly from the shorter moderately-extreme precipitation events, which corresponds to K in x- and y- direction of the fractured rock formation being higher and water being discharged to the river more rapidly. In contrast, longer duration moderately-extreme precipitation events caused a more prolonged response in the watershed, including the river levels. These higher river levels then force groundwater to be stored rather than discharged, thus enhancing the importance of storativity of the fractured rock formation.

As each scenario provided a different calibrated model, the results between them also differ. Based on R^2 values (Table 6), the calibration parameters of Scenario C provide the most similar trends to the observed data and that scenario is the only simulation that provides even a fair correlation to the observed trends. However, the RMSE for Scenario C is the highest of all the scenarios (Table 7) indicating that it did not match the magnitudes as well as the other scenarios. All of the scenarios have significant mismatch between model results and observed data at both MW-6 (Fig. 11a) and MW-7 (Fig. 11b) but are much closer for MW-7. Scenario A and Scenario B have nearly identical results, while Scenario D has the same patterns as Scenario A but with slightly lower hydraulic heads, and therefore greater RMSE (Table 7).

Table 6 Coefficient of determination (R^2) for all calibration scenarios.

Well ID	**a. base scenario**	**b. 2nd only (Feb 2018)**	**c. 1st only (Apr 2017)**	**d. No events**
MW-6	0.01	0.01	0.38	0.01
MW-7	0.91	0.91	0.94	0.93

Table 7 The Root Mean Squared Error (RMSE) for all calibration scenarios.

Well ID	**a. base scenario**	**b. 2nd only (Feb 2018)**	**c. 1st only (Apr 2017)**	**d. No events**
MW-6	3.25	3.25	5.60	3.99
MW-7	4.21	4.21	4.71	4.37

a.

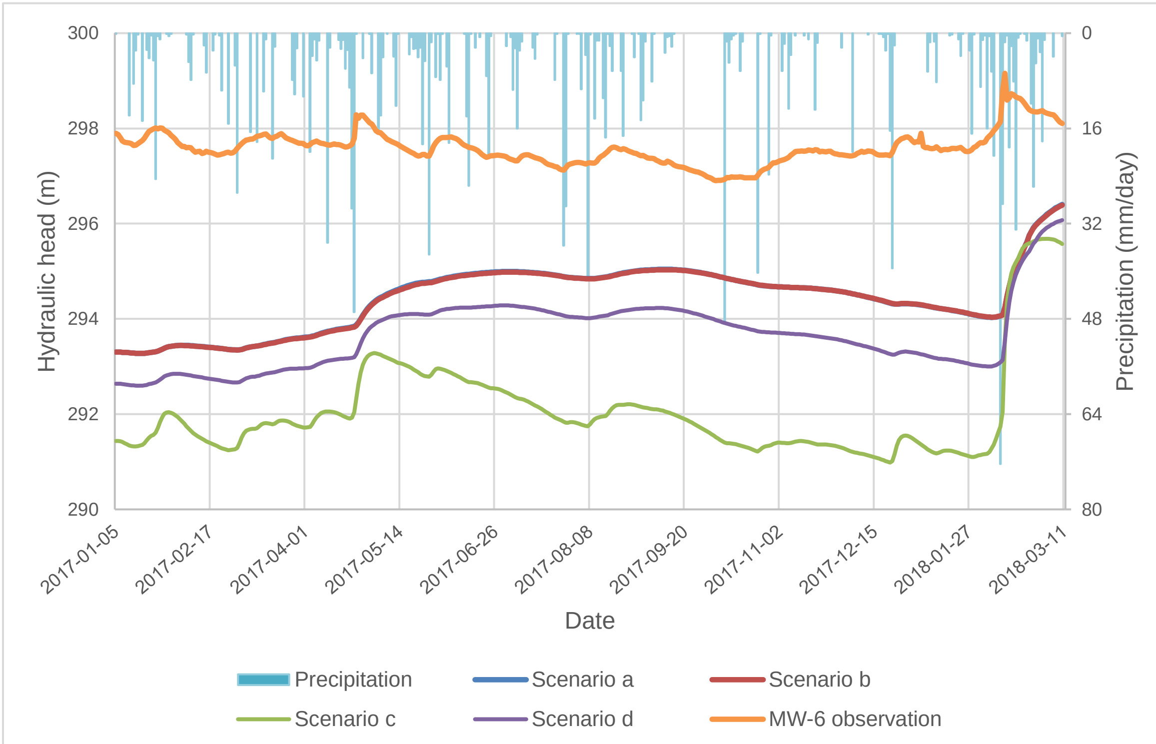

b.

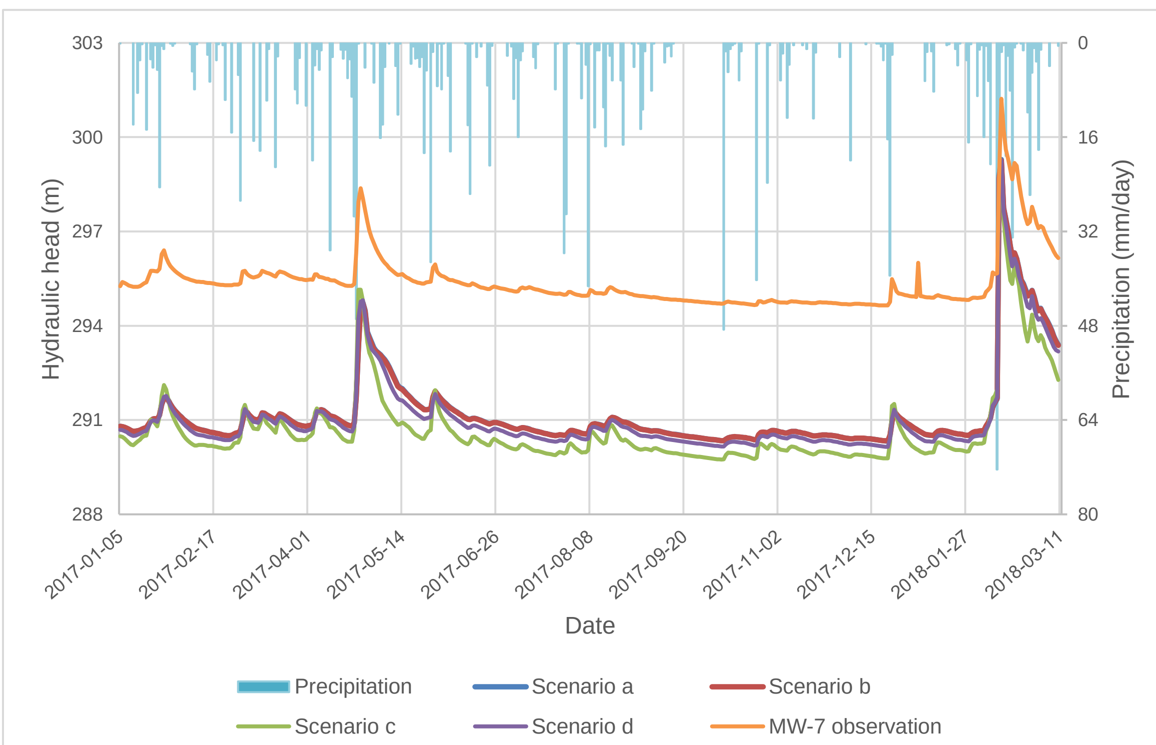

Fig. 11 Hydrograph during the observation period with the model simulations based on all four scenario calibrations and the observation from Sherman (2019) a. MW-6 b. MW-7

4.3 Future Scenario

It is predicted that by the end of the 21st century, the climate in Kentucky will become moderately wetter and warmer (U.S. Global Change Research Program [USGCRP], 2018). Annual precipitation may increase by 2.5-5%, with increased potential for extreme precipitation events, while annual ET may also increase 5-10% due to increased temperatures (Chattopadhyay et al., 2017; EPA, 2016; USGCRP, 2018). Here, we use the HLDTC model with calibrated parameters from Scenarios A and C (the base scenario and the scenario with the highest R^2) with +5% (1.768×10^{-8} m/s) and -5% (1.600×10^{-8} m/s) annual average precipitation. Both models were run until steady state was reached (simulated for 100 years). These simulations demonstrate how different future predictions on water availability would change with differing calibration datasets.

Head differences between Future Scenarios A and C indicate significant differences in water availability, as demonstrated by the differences in hydraulic head (Fig. 12). While the overall trends in hydraulic head across the domain are similar for both future cases, Future Scenario A has higher water levels than Future Scenario C, which is consistent with the calibration results (Fig. 11). The near surface layer has the least changes between Future Scenarios A and C, since the topsoil properties were the same for both of them. Beneath topsoil, the differences in hydraulic head decrease moving towards the river, from a maximum of 4 m around the ridge to 1 m near the riverbank. These results are consistent with the results discussed in section 4.2. In Future Scenario C, the change in K results in less vertical but more lateral flows through the fractured rock formation, causing more water to flow to the stream rather than being stored in the rock as in Future Scenario A. It is clear from these results that the inclusion of extreme events in calibration datasets does influence projections of future water availability.

a.

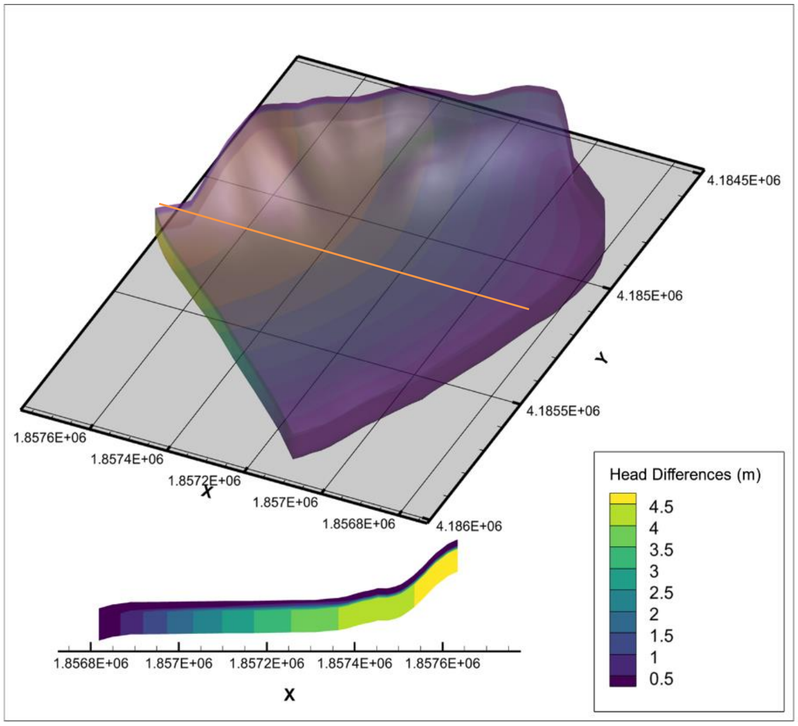

b.

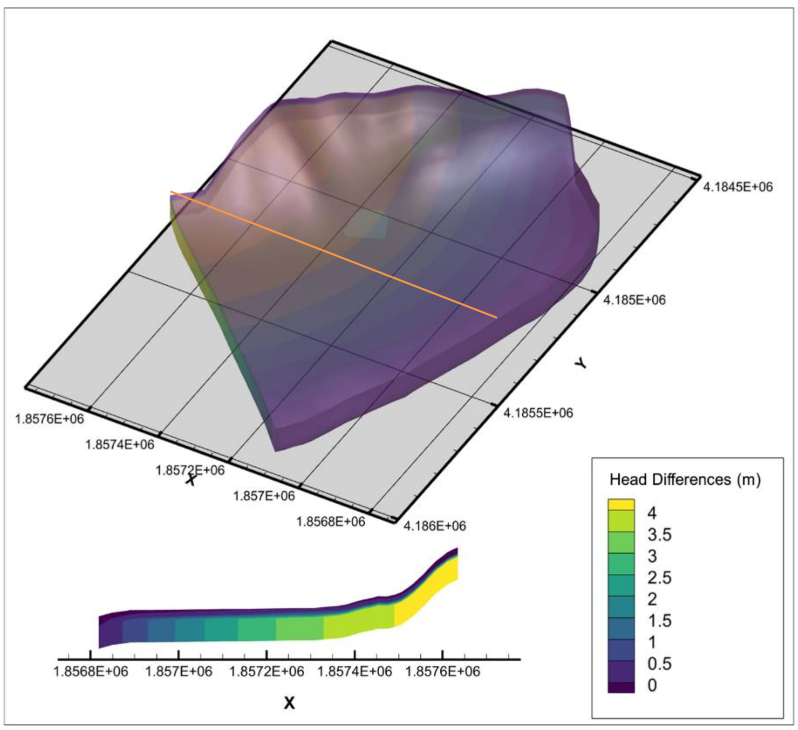

Fig. 12 Hydraulic head differences in future climates between models with calibrated parameters from Scenario a and c a. Future +5% b. Future -5%

Chapter 5
Conclusions

An integrated hydrologic model of the HLDTC site was developed using HGS and calibrated with PEST. This model was then calibrated with four different observation datasets: **a.** the entire observation record, including the two moderately-extreme precipitation events (base scenario), **b.** the entire observation record minus the 1st event (April 2017), **c.** the entire observation record minus the 2nd event (February 2018), and **d.** the observation record without either event.

Calibration parameters for this research are surface friction coefficient, hydraulic conductivity (K) of the topsoil, clayey sand, and fractured rock layers, and specific storage (S_S) of the clayey sand and fractured rock. The results demonstrate that the inclusion of observations responding to extreme precipitation events impacts the calibration of the hydrologic model. The model constructed by this study can better capture the response to shorter-duration moderately-extreme precipitation events, demonstrated by a better match between observed and simulated hydraulic heads in the scenario that includes only the shorter duration event. The variations in K and S_S were the highest between the base scenario and alternative scenarios of all the calibration parameters tested, with K having more variability than S_S. K changes in the alternative scenario for both the clayey sand and fractured rock layers; it has the greatest decrease in lateral K (x and y direction) of the clayey sand layers in Scenario D, and greatest increase in lateral K of fractured rock formation in Scenario C. S_S changed in the fractured rock formation in Scenario B. These results indicate that the inclusion of both precipitation events provides information about faster flow conditions for vertical groundwater flow of both formations. Additionally, short duration moderately-extreme precipitation events informed the model of faster lateral flow in the fractured rock formation, while longer duration moderately-extreme precipitation events informed the model of greater storativity in the fractured rock formation. Overall, it is evident that not only the presence or absence of these events informs model calibration, but the timing and duration of these events influences the parameters it informs.

Due to model simplifications, computational constraints, and data limitations, observations from one of the two monitoring wells used in this work was not well represented by the model. Future work should develop a larger scale model of the site to better characterize lateral groundwater movement across the site, in addition to collecting additional data to better constrain subsurface boundary conditions. It is also suggested that this model could develop a solution that effectively estimates ET and reflects its seasonal variation pattern. As K shows the most variation in the calibration process, future work should focus on this parameter, particularly its anisotropy.

References

Aquanty Inc. (2018). *HydroGeoSphere. A three-dimensional numerical model describing fully-integrated subsurface and surface flow solute transport.*

Boretti, A., & Rosa, L. (2019). Reassessing the projections of the World Water Development Report. *Npj Clean Water, 2*(1). https://doi.org/10.1038/s41545-019-0039-9

Camporese, M., Paniconi, C., Putti, M., & Orlandini, S. (2010). Surface-subsurface flow modeling with path-based runoff routing, boundary condition-based coupling, and assimilation of multisource observation data. *Water Resources Research, 46*(2). https://doi.org/10.1029/2008WR007536

Chattopadhyay, S., Edwards, D. R., Yu, Y., & Hamidisepehr, A. (2017). An Assessment of Climate Change Impacts on Future Water Availability and Droughts in the Kentucky River Basin. *Environmental Processes, 4*(3), 477–507. https://doi.org/10.1007/s40710-017-0259-2

Condon, L. E., & Maxwell, R. M. (2019). Simulating the sensitivity of evapotranspiration and streamflow to large-scale groundwater depletion. *Science Advances, 5*(6), eaav4574–eaav4574. https://doi.org/10.1126/sciadv.aav4574

Davison, Hwang, H., Sudicky, E. A., Mallia, D. V., & Lin, J. C. (2018). Full coupling between the atmosphere, surface, and subsurface for integrated hydrologic simulation. *Journal of Advances in Modeling Earth Systems, 10*(1), 43–53. https://doi.org/10.1002/2017MS001052

Doherty, J., Hayes, D. and Muffels, C. (2021). PEST Model-Independent Parameter Estimation User Manual Part I: PEST, SENSAN and Global Optimisers.

EPA. (2016). What climate change means for Kentucky. U. S. Environmental Protection Agency report EPA 430-F-16-019. https://19january2017snapshot.epa.gov/sites/production/files/2016-09/documents/climate-change-ky.pdf

Grimaldi, S. Schumann, G. J. ‐ P., Shokri, A., Walker, J. P., & Pauwels, V. R. N. (2019). Challenges, opportunities, and pitfalls for global coupled hydrologic ‐ hydraulic modeling of floods. *Water Resources Research, 55*(7), 5277 – 5300. https://doi.org/10.1029/2018WR024289

Harbaugh, A.W. (2005). MODFLOW-2005, the U.S. Geological Survey modular ground-water model -- the Ground-Water Flow Process: *U.S. Geological Survey Techniques and Methods 6-A16.*

Holman, Rivas-Casado, M., Bloomfield, J. P., & Gurdak, J. J. (2011). Identifying non-stationary groundwater level response to North Atlantic ocean-atmosphere teleconnection patterns using wavelet coherence. *Hydrogeology Journal,* 2011;19(6):1269-1278. doi:10.1007/s10040-011-0755-9

Kentucky Geological Survey. (n.d.). Water fact sheet in Kentucky. Kentucky Geological Survey, University of Kentucky. https://www.uky.edu/KGS/education/factsheet/factsheet_water.pdf

Kuffour, B. N. O., Engdahl, N. B., Woodward, C. S., Condon, L. E., Kollet, S., & Maxwell, R. M. (2020). Simulating coupled surface-subsurface flows with ParFlow v3.5.0: Capabilities, applications, and ongoing development of an open-source, massively parallel, integrated hydrologic model. *Geoscientific Model Development*, *13*(3), 1373–1397. https://doi.org/10.5194/gmd-13-1373-2020

KyFromAbove. (2022). *Kentucky's aerial photography & elevation data program*. KyFromAbove. https://kyfromabove.ky.gov/

Lü, H., Wang, Q., Horton, R., & Zhu, Y. (2021). The response of the hydrogeosphere model to alternative spatial precipitation simulation methods. *Water (Basel)*, *13*(14), 1891–. https://doi.org/10.3390/w13141891

Markstrom, S. L., Niswonger, R. G., Regan, R. S., Prudic, D. E., & Barlow, P. M. (2008). GSFLOW - coupled ground-water and surface-water flow model based on the integration of the precipitation-runoff modeling system (PRMS) and the modular ground-water flow model

(MODFLOW-2005). *U. S. Geological Survey Techniques and Methods 6-D1*. https://doi.org/10.3133/tm6d1

Maxwell, R. M., Woodward, C. S., Smith, S. G., Condon, L. E., & Kollet, S. J. (2023). *PARFLOW user's manual.* ParFlow User's Manual - ParFlow 3.12.0 documentation. https://parflow.readthedocs.io/en/latest/index.html

Meehl, G. A., Zwiers, F., Evans, J., Knutson, T., Mearns, L., & Whetton, P. (2000). Trends in extreme weather and climate events: Issues related to modeling extremes in projections of future climate change. *Bulletin of the American Meteorological Society*, *81*(3), 427–436. https://doi.org/10.1175/1520-0477(2000)081<0427:tiewac>2.3.co;2

Merrick, N., & Merric, D. (2016). *AlgoMesh User Guide*. HydroAlgorithmics Pty Ltd.

Naz, B. S., Sharples, W., Ma, Y., Goergen, K., & Kollet, S. (2023). Continental-scale evaluation of a fully distributed coupled land surface and groundwater model, ParFlow-CLM (v3.6.0), over Europe. *Geoscientific Model Development*, *16*(6), 1617–1639. https://doi.org/10.5194/gmd-16-1617-2023

Niu, G. Y., Paniconi, C., Troch, P. A., Scott, R. L., Durcik, M., Zeng, X., Huxman, T., & Goodrich, D. C. (2014). An integrated modelling framework of catchment-scale ecohydrological processes: 1. Model description and tests over an energy-limited watershed. *Ecohydrology, 7*(2), 427–439. https://doi.org/10.1002/eco.1362

Powell, J., & Reinhard, S. (2016). Measuring the effects of extreme weather events on yields. *Weather and Climate Extremes, 12*, 69-79. https://doi.org/10.1016/j.wace.2016.02.003.

Regan, R.S. & Niswonger, R.G. (2021). GSFLOW version 2.2.0: Coupled Groundwater and Surface-water FLOW model: U.S. Geological Survey Software Release, 18 February 2021.

Schewe, J., Gosling, S. N., Reyer, C., Zhao, F., Ciais, P., Elliott, J., Francois, L., Huber, V., Lotze, H. K., Seneviratne, S. I., van Vliet, M. T. H., Vautard, R., Wada, Y., Breuer, L., Büchner, M., Carozza, D. A., Chang, J., Coll, M., Deryng, D., … Warszawski, L. (2019). State-of-the-art global models underestimate impacts from climate extremes. *Nature Communications, 10*(1), 1005–1014. https://doi.org/10.1038/s41467-019-08745-6

Sherman, A. R., (2019). Temporal and spatial variability in groundwater flow and chemistry along the Cumberland River, Artemus, Kentucky. M.S. thesis, University of Kentucky, Lexington, USA. https://doi.org/10.13023/etd.2019.220

Sprinkle, C. L., Davis, R. W., & Mull, D. S. (1983). Evaluation of ground-water quality data from Kentucky. *U. S. Geological Survey Water-Resources Investigations Report 83-4240*.

Tong, X., Illman, W. A., Berg, S. J., & Ning, L. (2021). Hydraulic tomography analysis of municipal-well operation data with geology-based groundwater models. *Hydrogeology Journal*, *29*(5), 1979-1997. https://doi.org/10.1007/s10040-021-02320-4

U.S. Global Change Research Program (USGCRP). (2018). Fourth National Climate Assessment: Chapter 19: Southeast. https://nca2018.globalchange.gov/chapter/19/

USGS. (2017). *1 meter Digital Elevation Models (DEMs) - USGS National Map 3DEP Downloadable Data Collection*. U.S. Geological Survey. Retrieved March 25, 2022, from https://www.sciencebase.gov/catalog/item/543e6b86e4b0fd76af69cf4c

USGS. (2019). *The distribution of water on, in, and above the Earth*. U.S. Geological Survey. https://www.usgs.gov/media/images/distribution-water-and-above-earth

Weatherbase. (n.d.). *Artemus, Kentucky travel weather averages (Weatherbase)*. Weatherbase. Retrieved January 9, 2022, from https://www.weatherbase.com/weather/weather.php3?s=183051&cityname=Artemus-Kentucky-United-States-of-America.

Wu, B., Wang, S., Wang W., & An Y. (2019). Impact of future climate change on water resources in the arid regions of Northwest China based on surface water-groundwater coupling model: A case study of the middle reaches of the Heihe River. *Geology in China*, *46*(2), 369-380. https://doi.org/10.12029/gc20190213

Yang, C., Tijerina-Kreuzer, D. T., Tran, H. V., Condon, L. E., & Maxwell, R. M. (2023). A high-resolution, 3D groundwater-surface water simulation of the contiguous US: Advances in the integrated ParFlow CONUS 2.0 modeling platform. *Journal of Hydrology 626B*, 130294. https://doi.org/10.1016/j.jhydrol.2023.130294

Appendix A

Well log of MW-6

Technician A. Sherman, G. Wallas
Date 6/7/2017
Core MW6-1
Depth 0-4.8ft

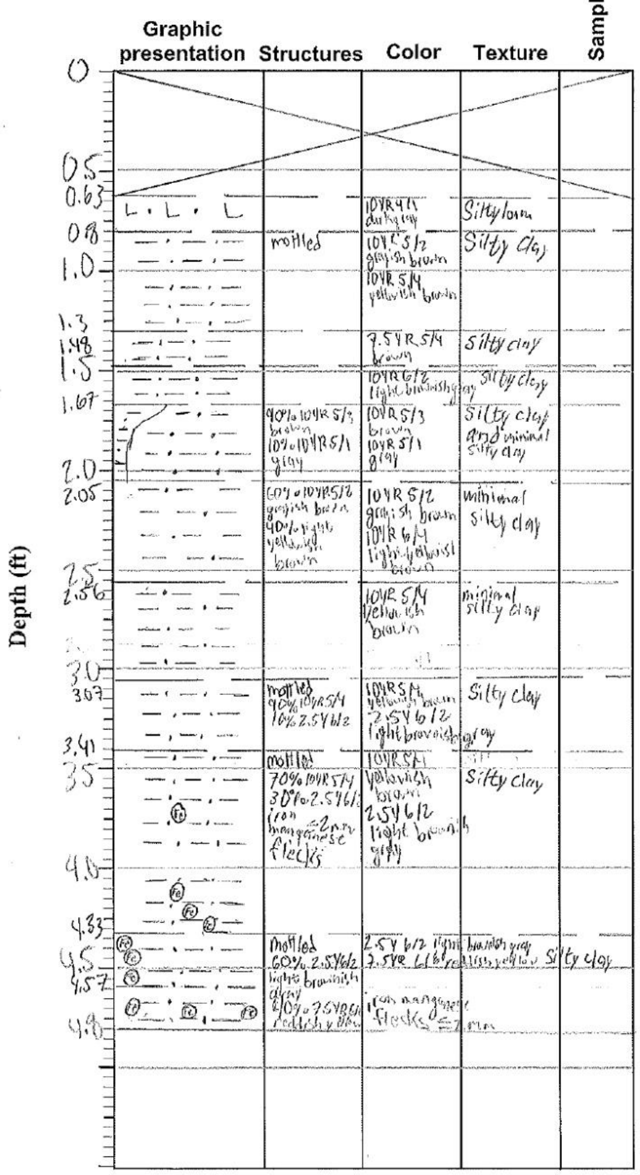

no recovery

There was no recovery from 0 to 0.63ft. Dark gray silty loam clearly changed to mottled grayish brown and yellowish brown silty clay. It had a color change to brown silty clay. It then clearly changed to light brownish gray silty clay. It abruptly changed to 90% brown silty clay and 10% gray minimal silty clay. It gradually changed to 60% grayish brown and 40% light yellowish brown minimal silty clay. It gradually changed to yellowish brown minimal silty clay. It abruptly transitioned to mottled 90% yellowish brown and 10% light brownish gray silty clay. At 3.41, more light brownish gray was in the soil. There was also iron oxidation: less than or equal to 2 millimeters. At 4.33, the soil changed to 60% light brownish gray and 40% reddish yellow silty clay with coal.

Technician A. Sherman, G. Valles
Date 6/8/2017
Core MLJ6-2
Depth 4.8-9.6 ft

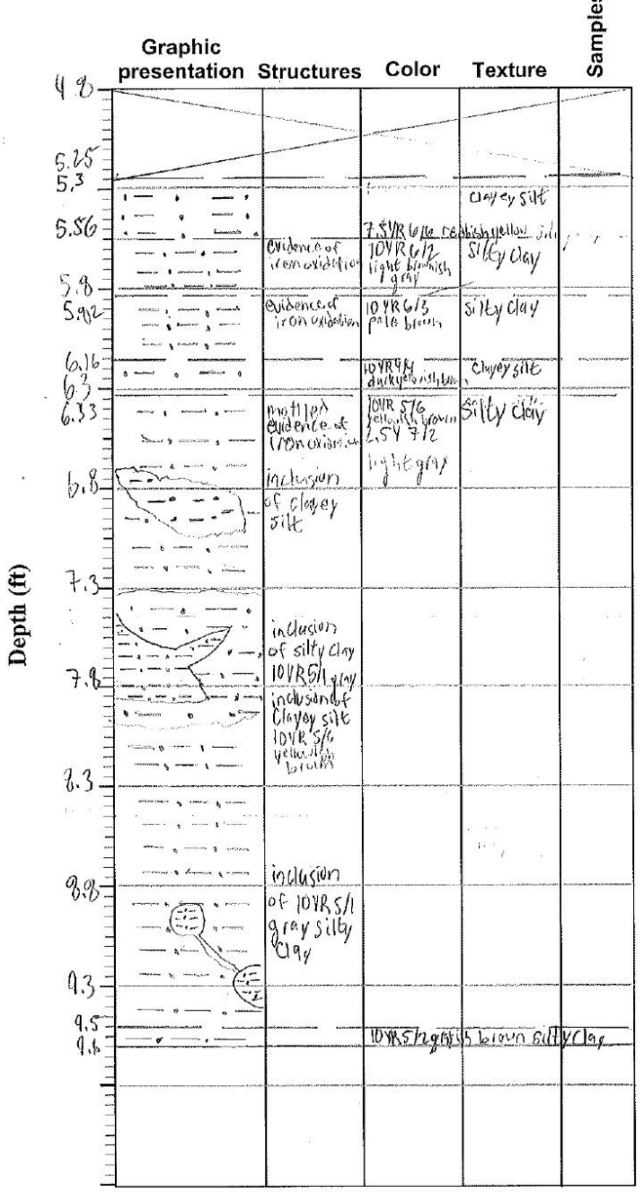

no recovery

There was no recovery from 4.8 to 5.25 ft. Reddish yellow clayey silt gradually changed to light brownish gray silty clay with evidence of iron oxidation. It clearly had a color change to pale brown. The soil gradually changed to dark yellowish brown clayey silt. It then gradually changed to mottled silty clay with inclusions of clayey silt, gray silty clay, yellowish brown clayey silt, and gray silty clay. The silty clay was equally mottled between yellowish brown and light gray. There was also evidence of iron oxidation. At 9.5 it abruptly changed to grayish brown silty clay.

Technician A. Sherman, G. Walles
Date 6/9/2017
Core MW6-3
Depth 9.6 - 14.4 ft

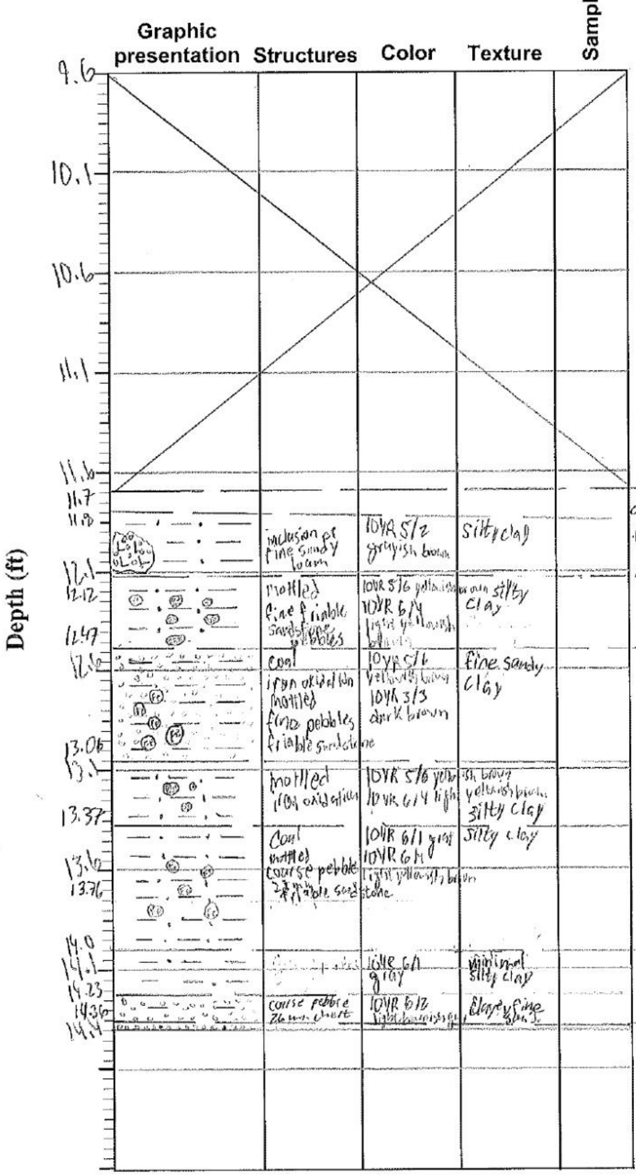

no recovery

drag-down There was no recovery from 9.6 to 11.7 ft. There was drag down from 11.7 ft to 11.9 ft.
There was grayish brown silty clay with an inclusion of fine sandy loam. It clearly changed to mottled yellowish brown and light yellowish brown silty clay with fine friable sandstone pebbles. It gradually changed to mottles yellowish brown and dark brown fine sandy clay. There was iron oxidation and fine pebbles of friable sand stone. It gradually changed to mottled yellowish brown and light yellowish brown silty clay. It diffused into mottled gray and light yellowish brown silty clay. There was a 27mm coarse pebble consisting of friable sandstone. It clearly changed to gray minimal silty clay. It clearly transitions to light brownish gray clayey fine sand. The core ended in strong brown silt & fine sand.

10YR 5/6 strong brown silty fine sand

Technician A. Sherman, G. Walles
Date 6/7/2017
Core MW6-4
Depth 14.4-19.2ft

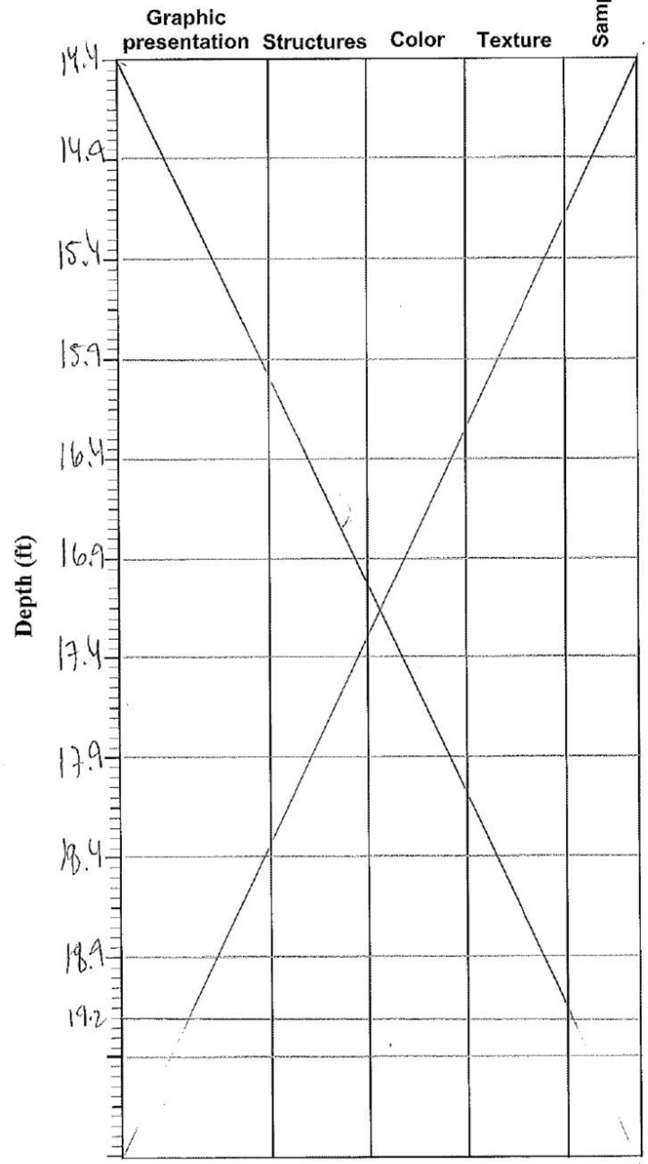

no recovery 14.4 to 19.2 ft
driller forgot to pull up
core

Technician A. Sherman, G. Valles
Date 6/9/2017
Core MW6-5
Depth 19.2 - 24ft

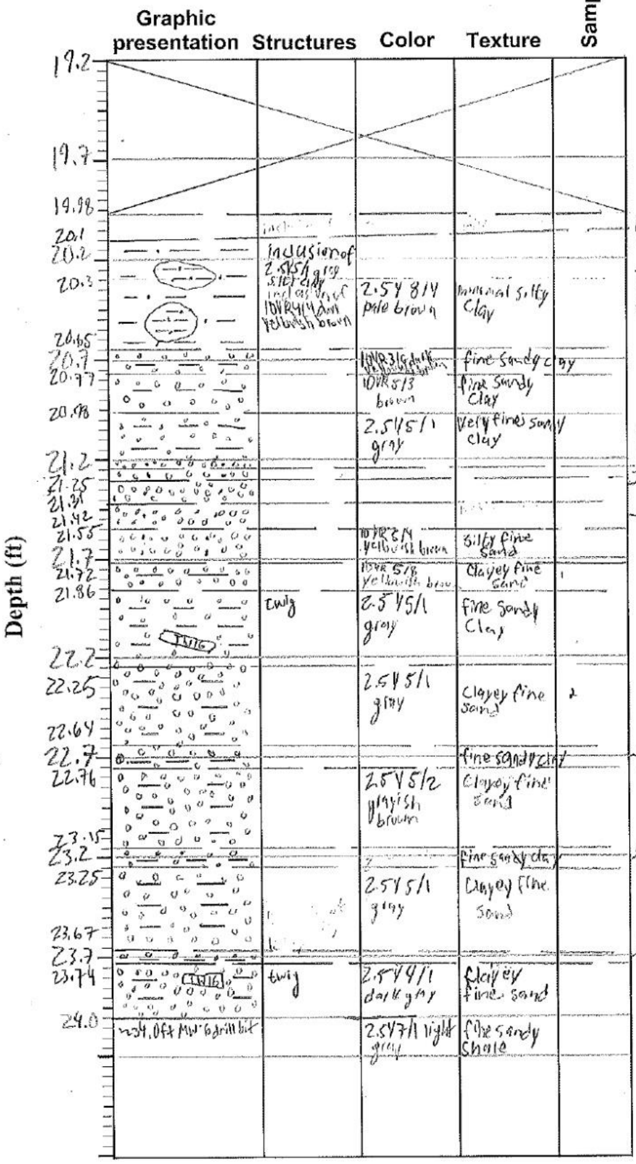

no recovery

potential drag-down

There was no recovery from 19.2 to 19.98 ft. There was potential drag-down from 19.98 to 20.1. The soil was pale brown minimal silty clay with an inclusion of gray silty clay and dark yellowish brown silty clay. It abruptly changed to dark yellowish brown fine sandy clay. It gradually changed to brown fine sandy clay. It diffused into gray very fine sandy clay. It gradually changed to brown silty fine sand. It gradually changed to yellowish brown silty fine sand. There was a gradual color change to brown. The soil gradually changed color to yellowish brown silty fine sand. It gradually changed to yellowish brown clayey fine sand. It abruptly transitioned to gray clayey fine sand. There was a gradual texture change to fine sandy clay. It abruptly changed to grayish brown clayey fine sand. It clearly changed to gray fine sandy clay. It clearly transitioned to gray clayey fine sand. It abruptly changed to gray fine sandy clay. It abruptly changed to dark gray clayey fine sand.

10YR 5/3 brown silty fine sand

10YR 5/6 yellowish brown silty fine sand

10YR 5/3 brown silty fine sand

2.5Y 5/1 gray

2.5Y 5/1 gray

fine sandy clay 2.5Y 5/1 gray

Appendix B

Well log of MW-7

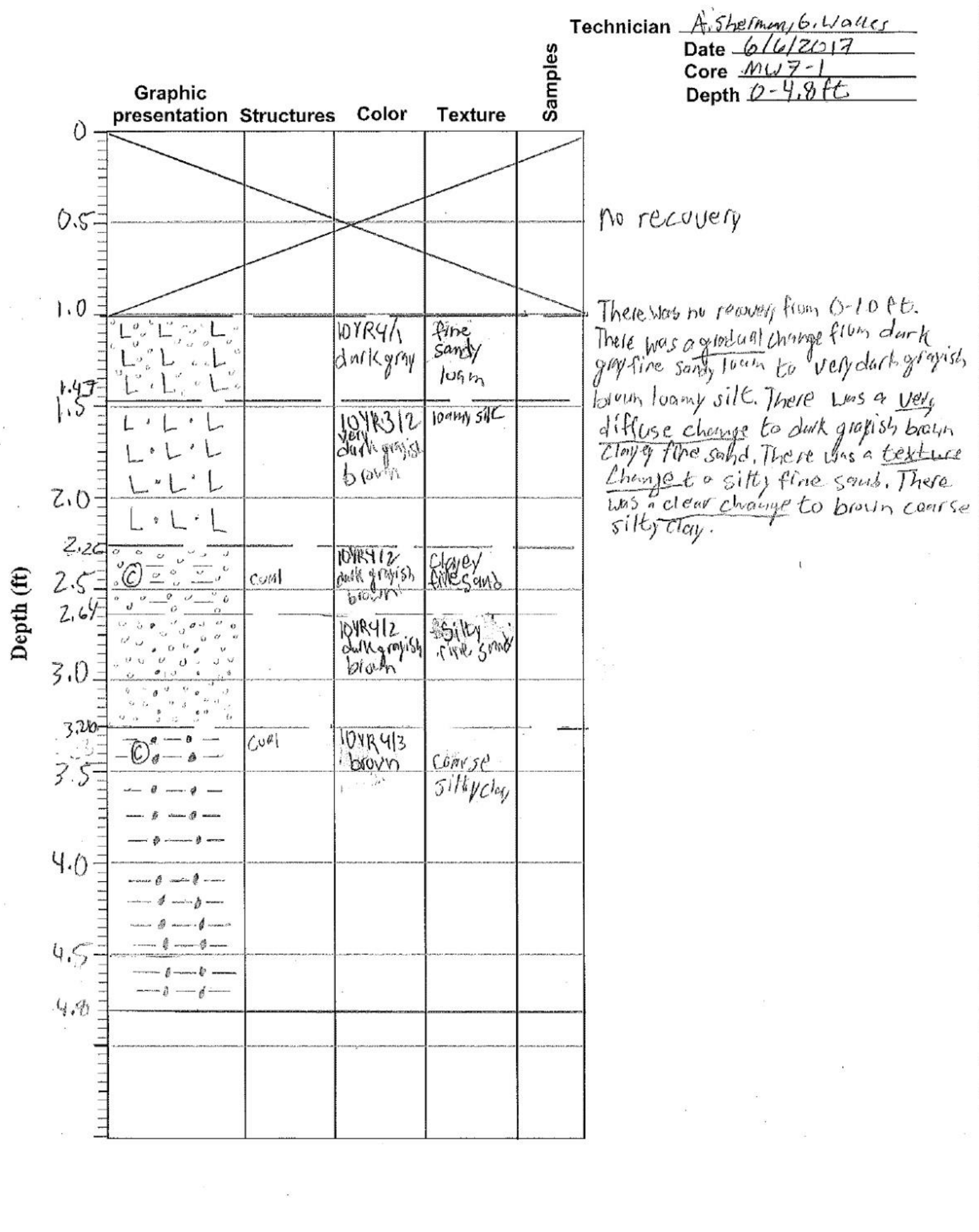

Technician A. Sherman, G. Walles
Date 6/6/2017
Core MW7-2
Depth 4.8 - 9.6 ft

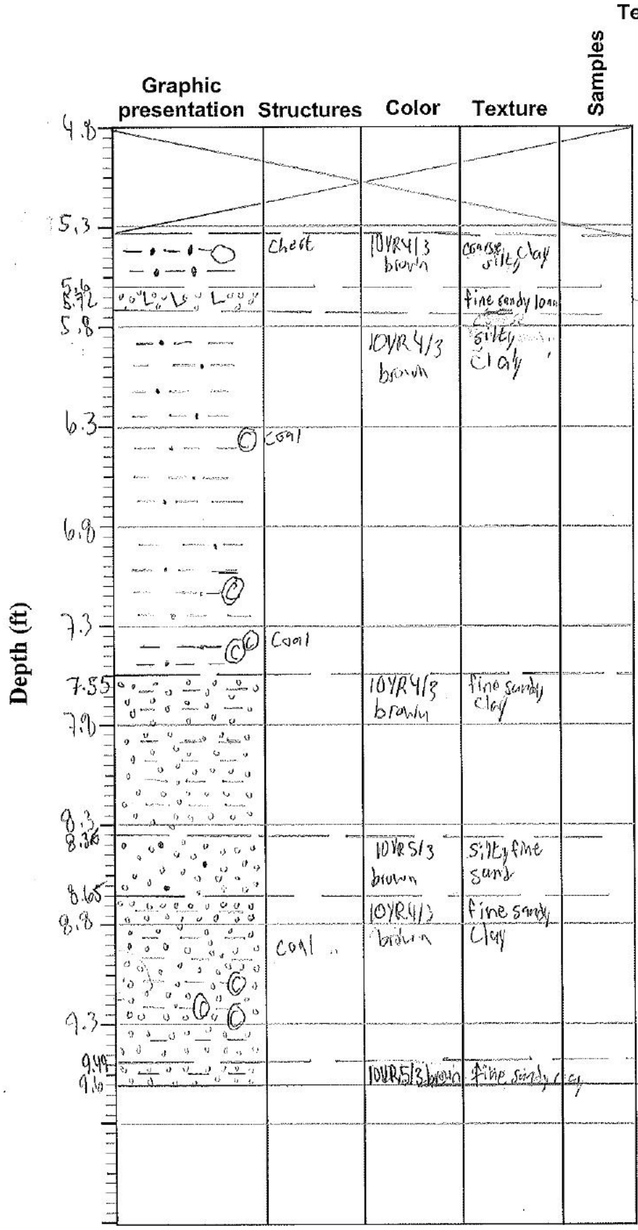

no recovery

10YR 3/2 very dark grayish brown

There was no recovery from 4.8 ft. to 5.33 ft. There was a gradual change from brown coarse silty clay to very dark grayish brown fine sandy loam. It then clearly changed to brown silty clay with coal. It clearly changed to brown fine sandy clay. Then, the soil abruptly changed to brown silty fine sand. The soil gradually changed to brown fine sandy clay. The soil was a brown fine sandy clay at the end.

Technician A. Sherman/ G. Valles
Date 6/6/2017
Core MW7-3
Depth 9.6-14.4ft

Depth (ft)	Graphic presentation	Structures	Color	Texture	Samples
9.6					
10.1					
10.6					
11.1					
11.6					
11.9					
12.1					
12.15		Coal	10YR4/3 brown	silty clay	
12.6					
13.0		coal	10YR5/4 yellowish brown	Clayey fine sand	
13.1					
13.55					
13.6		Coal	10YR5/4 yellowish brown	Clayey fine sand	
14.05					
14.1			10YR5/4 yellowish brown	Silty fine sand	
14.25			10YR4/4 dark yellowish brown	fine sandy clay	
14.4					

no recovery

drag-down

There was no recovery from 9.6ft to 11.9ft. There was drag-down from 11.9ft to 12.15 ft. Brown silty clay with coal gradually changed to yellowish brown clayey fine sand. It clearly changed to yellowish brown clayey fine sand. This abruptly changed to yellowish brown silty fine sand. It abruptly changed to dark yellowish brown fine sandy clay.

Technician A. Sherman, G. Valles
Date 6/7/2017
Core MU7-4
Depth 14.4-19.2ft

Depth (ft)	Graphic presentation	Structures	Color	Texture	Samples
14.4 – 15.9 (14.4, 14.9, 15.4, 15.9)					
15.9 – 15.98					
15.98 – 16.4		60% 10YR5/4 yellowish brown 40% 10YR5/2 grayish brown	10YR5/2 grayish brown 10YR 5/4	very fine sandy clay	
16.4 – 16.67		Coal	yellowish brown		
16.67 – 17.02 (16.9)		80% 10YR4/1 dark gray 20% 10YR 5/4 yellowish brown	10YR4/1 dark gray 10YR 5/4 yellowish brown	fine sandy loam	
17.02 – 17.29			10YR5/4 yellowish brown	fine sandy clay	
17.29 – 17.52 (17.4)		inclusion of fine sandy clay	10YR5/4 yellowish brown	clayey medium sand	
17.52 – 17.9 (17.85)			10YR 5/4 yellowish brown	minimal coarse silty clay	
17.9 – 18.4 (18.3)			10YR5/4 yellowish brown	fine sandy clay	
18.4 – 18.42		iron oxidation	10YR5/4 yellowish brown	very fine sandy clay	
18.42 – 19.02 (18.9)		evidence of iron oxidation coal	10YR 5/4 yellowish brown	fine sandy clay	
19.02 – 19.2			10YR 5/4 yellowish brown	fine sandy clay	

no recovery

10YR 3/2 very dark grayish brown
very fine sandy loam

There was no recovery from 14.4ft to 15.9ft. At the top of the core there was very dark grayish brown very fine sandy loam. It clearly changed to grayish brown and yellowish brown very fine sandy clay. Approximately 60% of the core was yellowish brown and 40% was grayish brown. It clearly changed to dark gray and yellowish brown fine sandy loam. Approximately 80% of it was dark gray fine sandy loam and 20% was yellowish brown very fine sandy clay. It gradually changed to yellowish brown fine sandy clay. It abruptly transitioned to yellowish brown clayey medium sand with inclusions of fine sandy clay. This abruptly changed to minimal coarse silty clay. There was a clear change to fine sandy clay. After that there was an abrupt change to very fine sandy clay. There was another texture change to fine sandy clay, and finally a clear change to fine sandy clay.

Technician A. Sherman, G. Walles
Date 5/31/2017
Core MW7-5
Depth 19.2-24

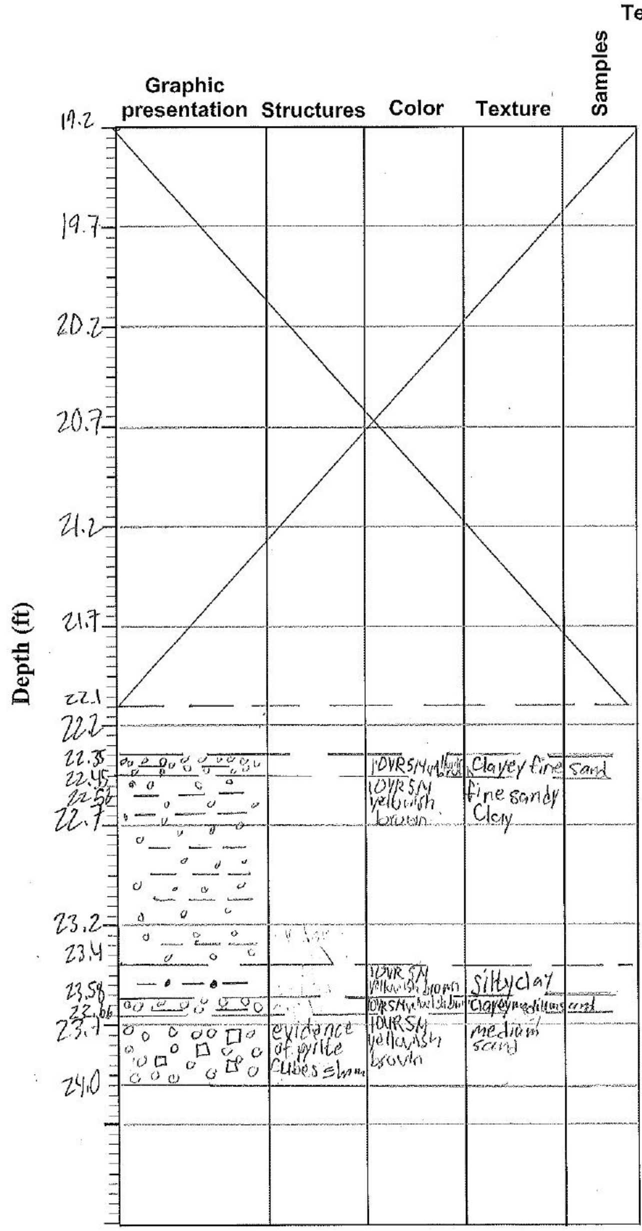

no recovery

possible drag-down because of lack of structure and loam after so long of not seeing loam

There was no recovery from 19.2 feet to 22.1 feet. There were texture changes but no color changes. The core was yellowish brown. Clayey fine sand abruptly changed to fine sandy clay. It abruptly changed to silty clay. It clearly changed to clayey medium sand and ~~gradually~~ transitioned to medium sand with pyrite cubes smaller than one millimeter.

Technician A.Shelman/G.Walles

Date 8/2/2017

Core MW7 Bay Samples

Depth 25.6-36.5ft

Depth (ft)

Graphic presentation	Structures	Color	Texture	Samples
~25.6ft MW7-6a ~27.2ft MW7-6b		10YR4/4 dark yellowish brown 10YR4/3 brown	Clayey silt clayey coarse silt	
~30.4ft MW7-7a ~32.0ft MW7-7b ~41.5ft MW7 drill	bit	10YR4/3 brown 10YR7/3 [illegible] GLEY1 4/N dark gray	Silty fine sand silt Clayey shale	
~41.5 ft MW7 rock	Sample-shale well bottom	GLEY1 4/N dark gray	Silty shale	